



University of Warwick institutional repository: <http://go.warwick.ac.uk/wrap>

This paper is made available online in accordance with publisher policies. Please scroll down to view the document itself. Please refer to the repository record for this item and our policy information available from the repository home page for further information.

To see the final version of this paper please visit the publisher's website. Access to the published version may require a subscription.

Author(s): Laurencin, Danielle, Almora-Barrios, Neyvis, de Leeuw, Nora H., Gervais, Christel, Bonhomme, Christian, Mauri, Francesco, Chrzanowski, Wojciech, Knowles, Jonathan C., Newport, Robert J., Wong, Alan, Gan, Zhehong and Smith, Mark E.

Article Title: Magnesium incorporation into hydroxyapatite

Year of publication: 2011

Link to published article :  
<http://dx.doi.org/10.1016/j.biomaterials.2010.11.017>

Publisher statement: NOTICE: this is the author's version of a work that was accepted for publication in Biomaterials. Changes resulting from the publishing process, such as peer review, editing, corrections, structural formatting, and other quality control mechanisms may not be reflected in this document. Changes may have been made to this work since it was submitted for publication. A definitive version was subsequently published in Biomaterials, 32(7), pp. 1826-1837. Doi: 10.1016/j.biomaterials.2010.11.017

# Magnesium incorporation into hydroxyapatite

## Authors

Danielle Laurencin,<sup>a,1,\*</sup> Neyvis Almora-Barrios,<sup>b</sup> Nora H. de Leeuw,<sup>b,\*</sup> Christel Gervais,<sup>c</sup> Christian Bonhomme,<sup>c</sup> Francesco Mauri,<sup>d</sup> Wojciech Chrzanowski,<sup>e,2</sup> Jonathan C. Knowles,<sup>e,f</sup> Robert J. Newport,<sup>g</sup> Alan Wong,<sup>a,3</sup> Zhehong Gan,<sup>h</sup> and Mark E. Smith<sup>a</sup>

## Affiliations

<sup>a</sup> Department of Physics, University of Warwick, Coventry, CV4 7AL, UK

<sup>b</sup> University College London, Department of Chemistry, 20 Gordon Street, London, WC1H 0AY, UK.

<sup>c</sup> UPMC Univ Paris 06, UMR CNRS 7574, Laboratoire de Chimie de la Matière Condensée de Paris, F-75005 Paris, France

<sup>d</sup> UPMC Univ Paris 06, UMR CNRS 7590 Institut de Minéralogie et Physique des Milieux Condensés, F-75015 Paris, France

<sup>e</sup> Eastman Dental Institute, University College London, 256 Gray's Inn Road, London, WC1X 8LD, UK

<sup>f</sup> WCU Research Centre of Nanobiomedical Science, Dankook University, San#29, Anseo-dong, Dongnam-gu, Cheonan-si, Chungnam, 330-714, South Korea

<sup>g</sup> School of Physical Sciences, Ingram Building, University of Kent, Canterbury, CT2 7NH, UK

<sup>h</sup> Center of Interdisciplinary Magnetic Resonance, National High Magnetic Field Laboratory, Tallahassee, Florida, FL32310, USA.

<sup>1</sup> Present address : Institut Charles Gerhardt de Montpellier, UMR 5253, CNRS-UM2-ENSCM-UM1,  
CC 1701, Place Eugène Bataillon, 34095 Montpellier cedex 5, France

<sup>2</sup> Present address: The University of Sydney, The Faculty of Pharmacy, Pharmacy and Bank Building  
Sydney, NSW, 2006.

<sup>3</sup> Present address : CEA Saclay, IRAMIS/SCM/LSDRM, Gif-sur-Yvette 91191, France.

\* Corresponding authors. Tel.: +33 4 67 14 38 02; Fax: +33 4 67 14 38 88. *Email address:*  
danielle.laurencin@univ-montp2.fr, n.h.deleeuw@ucl.ac.uk

## **Abstract**

The incorporation of Mg in hydroxyapatite (HA) was investigated using multinuclear solid state NMR, X-ray absorption spectroscopy (XAS) and computational modeling. High magnetic field  $^{43}\text{Ca}$  solid state NMR and Ca K-edge XAS of a ~10% Mg-substituted HA were performed, bringing direct evidence of the preferential substitution of Mg in the Ca(II) position.  $^1\text{H}$  and  $^{31}\text{P}$  solid state NMR show that the environment of the anions is disordered in this substituted apatite phase. Both Density Functional Theory (DFT) and interatomic potential computations of Mg-substituted HA structures are in agreement with these observations. Indeed, the incorporation of low levels of Mg in the Ca(II) site is found to be more favourable energetically, and the NMR parameters calculated from these optimized structures are consistent with the experimental data. Calculations provide direct insight in the structural modifications of the HA lattice, due to the strong contraction of the  $\text{M}\cdots\text{O}$  distances around Mg. Finally, extensive interatomic potential calculations also suggest that a local clustering of Mg within the HA lattice is likely to occur.

## **Keywords**

Hydroxyapatite

Magnesium

Solid State NMR

X-ray absorption Spectroscopy

Computer Modeling

Density Functional Theory

## Introduction

Calcium hydroxyapatite is the main mineral component of bone tissue and teeth. Its composition differs from that of synthetic hydroxyapatite  $\text{Ca}_{10}(\text{PO}_4)_6(\text{OH})_2$  (HA), due to the presence of several ionic substitutions in the lattice, such as  $\text{CO}_3^{2-}$ ,  $\text{F}^-$ ,  $\text{Mg}^{2+}$  and  $\text{Na}^+$ . [1-3] These minor species not only alter the space group, morphology, stability, and mechanical properties of the HA structure, but also play an important role in the biological responses of bone cells. For instance, carbonates have a strong influence on the growth of apatite crystals, [1] sodium plays a role in bone remodeling, [4] whereas fluoride prevents the development of dental caries. [5] These ions are distributed inhomogeneously throughout the tissue, and their concentration changes according to the age and maturity of the mineral. [1, 6, 7]

Magnesium is known to be an important trace element in bone and teeth. Indeed, despite its low concentration (generally between ~0.5 and 1.5 wt%), it plays a key role in bone metabolism, in particular during the early stages of osteogenesis where it stimulates osteoblast proliferation, [8] and its depletion causes bone fragility and bone loss. [9] Furthermore, relationships have been suggested between the magnesium content in enamel and the development of dental caries. [10]

Given the biological relevance of magnesium, many research teams have worked on the preparation of apatite and calcium-phosphate implant materials containing low levels of Mg, which has been shown to improve their bioactivity. [11, 12] Moreover, much work has been done on synthetic magnesium-substituted apatites (Mg-HA), in order to try to elucidate the exact structural role of Mg in bone. According to the literature, the replacement of calcium by magnesium in HA is limited. This is related to the large size difference between  $\text{Mg}^{2+}$  and  $\text{Ca}^{2+}$  (~0.28 Å difference in radius according to the Pauling scale), which leads to strong distortions of the HA lattice and reduces its crystallinity. These changes have a direct impact on the properties of Mg-HA, compared to their non-substituted analogues: [12-16] it notably increases their solubility and biodegradability in physiological fluids and favours their thermal conversion into substituted  $\beta$ -tricalcium phosphate ( $\beta\text{-Ca}_{3-x}\text{Mg}_x(\text{PO}_4)_2$ ). Additional studies have also shown that the co-substitution of other ions such as  $\text{CO}_3^{2-}$  in the structure

may help counteract the destabilization of the apatite phase [17] and that, according to the synthetic procedure or the age of the Mg-HA material, higher Mg concentrations at the surface of the HA crystallites can be observed.[18, 19]

Numerous spectroscopic techniques have been used to learn more about the substitution of magnesium in HA. Nevertheless, although X-ray diffraction,[20] X-Ray Photoelectron Spectroscopy,[14] and cathodoluminescence spectroscopy[21] clearly indicate that Mg enters the HA lattice, several key structural characteristics remain unsolved, and little is known about how exactly Mg-incorporation affects the bulk structure of apatites. In particular, the position of Mg in the HA lattice is still an open question: does it occupy one or both of the two crystallographic calcium sites, referred to as Ca(I) and Ca(II), which present different local environments, as depicted in Figures 1 and 2? Some authors state that Mg enters the Ca(II) site,[13] whereas others the Ca(I) site.[15, 21, 22] The main difficulty in answering this question in the case of Mg-HA arises from the absence of high resolution spectroscopic data over an important range of composition, and the significant loss of crystallinity of Mg-HA compounds above ~ 20% Mg. Thus, in contrast with Sr- or Ba-substituted HA,[23, 24] Rietveld analyses based on X-ray powder patterns are not conclusive for Mg-HA, and both the Ca(I)[15] and the Ca(II)[20] sites have been suggested to be the preferential site of incorporation of Mg. Such discrepancies might be due to differences in synthetic procedures (which could perhaps alter the final site for incorporated Mg), and/or to the low quality of the XRD patterns used in the Rietveld refinements. Indeed, it is noteworthy that some of the refined distances are surprising: for a sample with ~ 30% Mg, an average M···O bond distance was found that was almost identical to the non-substituted compound,[20] which seems contradictory with the fact that average Mg···O distances are generally ~0.4 Å shorter than average Ca···O distances and that there is a contraction of the HA lattice.[13] It thus appears necessary to find other analytical tools not only to help elucidate the structural and biological role of Mg, but also help shed light on the changes in local structure around the different atoms in the lattice.

Recently, alternative approaches have started to emerge to investigate in more depth the mode of incorporation of substituting divalent cations in HA phases. In particular, it has been shown that much information could be accessed experimentally using spectroscopic techniques which are sensitive to the local structure around particular cations, such as X-ray absorption spectroscopy and solid state NMR. For instance, the preferential incorporation of  $\text{Zn}^{2+}$  and  $\text{Pb}^{2+}$  into the Ca(II) site of apatites has been demonstrated using Zn K-edge EXAFS and XANES,[25] and  $^{207}\text{Pb}$  solid state NMR,[26] respectively. Furthermore, an increasing number of computational studies are reported aimed at determining any energetic advantages of incorporating impurity ions into different sites of the HA lattice, [27-30] and it has been shown that these can bring further insight into the structural changes in substituted species, and help understand spectroscopic data.[25]

In the case of Mg-substituted apatites, no experimental NMR or XAS data have been reported so far, and the first computational studies were published very recently.[28] Using Density Functional Theory (DFT) calculations, Matsunaga *et al.* showed that the incorporation of  $\text{Mg}^{2+}$  is more favourable in the Ca(II) than in the Ca(I) site, and that it induces strong changes in the position of the coordinated oxygen atoms. However, no experimental evidence could be referred to to confirm the changes in the local structure around the different ions in the structure: the experimental data available so far for Mg-HA are insufficient (*i*) to validate the computational models developed for these systems, and (*ii*) to show how Mg modifies the bulk and surface structure of apatite crystallites and thereby modifies the biological responses. The purpose of this work was thus to investigate the structure of Mg-HA systems at the *molecular level*, using techniques which are sensitive to the *local* environment of the atoms, such as multinuclear solid state and X-ray absorption spectroscopy, and to discuss the experimental and spectroscopic data in view of computational models of Mg-HA. The local structure around all the ions in the structure, and notably magnesium and calcium, was analysed in order to try to derive sound conclusions on the structure of these phases.

## Materials and methods

### *Synthesis*

Hydroxyapatite  $\text{Ca}_{10}(\text{PO}_4)_6(\text{OH})_2$  (HA) and magnesium-substituted hydroxyapatite  $\text{Ca}_{10-x}\text{Mg}_x(\text{PO}_4)_6(\text{OH})_2$  (Mg10-HA) were prepared following a precipitation method adapted from the literature.[31] High purity calcium nitrate tetrahydrate ( $\text{Ca}(\text{NO}_3)_2 \cdot 4\text{H}_2\text{O}$ , Alfa Aesar), magnesium nitrate hexahydrate ( $\text{Mg}(\text{NO}_3)_2 \cdot 6\text{H}_2\text{O}$ , Aldrich) and ammonium dihydrogen phosphate ( $\text{NH}_4\text{H}_2\text{PO}_4$ , Aldrich) were used as starting materials. All reactions were performed in freshly distilled water and under an  $\text{N}_2$  atmosphere, in order to avoid the incorporation of carbonates in the HA lattice.

HA was prepared by heating an aqueous solution of calcium nitrate to  $90^\circ\text{C}$  ( $[\text{Ca}^{2+}] = 0.216 \text{ mol.L}^{-1}$ ,  $V = 100 \text{ mL}$ , pH adjusted to 10.0 with a  $1 \text{ mol.L}^{-1}$  solution of  $\text{NH}_4\text{OH}$ ), and adding dropwise under stirring an aqueous solution of ammonium dihydrogen phosphate ( $C = 0.130 \text{ mol.L}^{-1}$ ,  $V = 100 \text{ mL}$ , pH adjusted to 10.0 by addition of concentrated  $\text{NH}_4\text{OH}$ ). This leads to the progressive precipitation of a white solid. The suspension was stirred at  $90^\circ\text{C}$  (temperature of the oil bath) for a total time of 5 hours, during which small amounts of concentrated  $\text{NH}_4\text{OH}$  were added, in order to keep the pH above 9.0. The reaction medium was then left to cool at room temperature, and centrifuged in order to separate the white precipitate (10000 rpm for 10 min). The solid was washed four times with freshly distilled water, and then dried at  $100^\circ\text{C}$  under vacuum overnight (yield > 85%). In the case of Mg10-HA, the same synthetic procedure was followed, but using a mixture of calcium and magnesium nitrate, with 10.0% magnesium with respect to the total cationic concentration.

### *General characterization*

Elemental analyses of Mg10-HA were performed (i) by ICP-AES by the Service Central d'Analyse of the CNRS (Vernaison, France), to determine the Ca, P and Mg contents, (ii) by ionic chromatography on a Dionex 1000 ICS system to measure the Ca and Mg contents, after dissolution of the samples in sulphuric acid.



SEM and EDXS (for Ca, P and Mg) studies were carried out on a Jeol 6100 Scanning Electron Microscope coupled to an EDAX Genesis analytical system. TEM and EDXS analyses (for Ca, P and Mg) were carried out on a Jeol 6100 Transmission Electron Microscope coupled to an EDAX Genesis analytical system. X-ray diffraction patterns were collected with a Bruker D8 Advance diffractometer using the CuK $\alpha$  radiation. Room temperature measurements were performed in the  $2\theta$  range between 10 and 70°. IR spectra were also recorded from KBr pellets on a Perkin Elmer GX FTIR spectrometer between 4000 cm<sup>-1</sup> and 400 cm<sup>-1</sup>. XRD, SEM and TEM data can be found in Figure S1 in the supplementary materials (from hereon, “S” will refer to supplementary information).

### *Solid state NMR*

<sup>1</sup>H and <sup>31</sup>P NMR experiments were carried out at 7.1 T on a Varian Infinity Plus 300 spectrometer, using a Bruker 4 mm MAS probe. Single-pulse magic angle spinning <sup>1</sup>H and <sup>31</sup>P NMR spectra were collected at a spinning rate of 10 kHz, using recycle delays of 10 s and 30 s respectively. In the case of <sup>31</sup>P, it was verified that the lineshape remains unaltered when increasing the recycle delay to 500 s. <sup>1</sup>H and <sup>31</sup>P chemical shifts were referenced using TMS (Si(CH<sub>3</sub>)<sub>4</sub>, resonance at 0 ppm) and NH<sub>4</sub>H<sub>2</sub>PO<sub>4</sub> (resonance at 0.9 ppm), respectively.

Natural abundance <sup>43</sup>Ca solid state NMR spectra were recorded at 18.8 T on a Varian Infinity Plus 800 spectrometer using a Varian 4 mm rotor probe spinning at 8 kHz, and at 19.6 T on a Bruker DRX 830 spectrometer using a 7 mm homebuilt probe spinning at 5 kHz. Recycle delays of 0.1 to 0.25 s were used, and 400000 to 1500000 transients were acquired, with experimental times ranging from 28 to 48 h (it is noteworthy that changing the recycle delays did not affect the final lineshapes). For the spectra recorded at 18.8 T, the rotor-assisted population transfer (RAPT) sequence (sets of +X/-X 2.5  $\mu$ s pulses with a  $\sim$  15 kHz radiofrequency field strength), [32, 33] which had previously been optimized for non-substituted hydroxyapatite, [34] was applied for sensitivity enhancement prior to a 90° pulse selective for the central transition. For the spectra recorded at 19.6 T, a 5 kHz chirp

sweep[35] was applied for sensitivity enhancement at ~250 kHz below the central transition frequency.  $^{43}\text{Ca}$  NMR chemical shifts were referenced using a 1 mol.L $^{-1}$  aqueous solution of  $\text{CaCl}_2$  (at 0 ppm).[36, 37] The conclusions from the data recorded at 19.6 T were identical to those at 18.8 T.

Natural abundance  $^{25}\text{Mg}$  NMR experiments were carried out at 19.6 T on a Bruker DRX 830 spectrometer using a 7 mm homebuilt probe spinning at 5 kHz. 240000 transients were acquired, with a recycle delay of 0.3 s.  $^{25}\text{Mg}$  NMR chemical shifts were referenced using an aqueous solution of magnesium sulfate.[38, 39]

### *Ca K-edge EXAFS and XANES*

EXAFS (Extended X-ray Absorption Fine Structure) and XANES (X-ray Absorption Near Edge Structure) measurements were performed on the XAFS BL11.1 beamline at the Elettra Sincrotrone, Trieste, Italy. Samples were ground to a fine powder, diluted in polyvinyl pyrrolidone (average molecular wt 40,000, Sigma-Aldrich, “PVP40”), pressed into pellets, and run at room temperature in transmission mode using ion chambers before and after the sample in order to measure incident and transmitted X-ray intensity. Spectra were collected at the Ca K-edge at 4038 eV. The Elettra ring energy was 2 GeV and the maximum ring current was 200 mA. The incident X-ray energy on the sample was defined using a two-crystal Si(111) monochromator detuned (by ~50%) to reduce higher energy harmonics. The instrument was evacuated to  $\sim 10^{-5}$  Pa in order to reduce X-ray losses due to attenuation in the air. An energy resolution of ~0.3 eV at the Ca K-edge was achieved, and the energy was calibrated using  $\text{CaF}_2$  as a calibrant placed between the transmission and a third ion chamber. For the XANES spectra, the pre-edge (3900–4017 eV), edge (4017–4100 eV) and post-edge (4100–4200 eV) regions were scanned in 5.0, 0.1 and 1.0 eV steps respectively, and dwell times per point of 1.0, 2.0 and 1.0 s respectively. For the EXAFS spectra, the pre-edge (3900–4017 eV), edge (4017–4100 eV) and post-edge (4100–4800 eV) regions were scanned in 5.0, 2.0 and 1.0 eV steps respectively, and dwell times per point of 1.0, 1.0 and 2.0 s respectively.

Data reduction was performed using the standard software packages Athena,[40] Viper2006[41, 42] and EXCURV98.[43] Typically, two XANES and three EXAFS data sets were collected for each sample, which were respectively averaged and normalized using Athena. All EXAFS spectra were background-subtracted using Viper2006, with a second order polynomial fitted to the pre-edge region and a polynomial spline (going through 7 knots) fitted to the post-edge region to describe the underlying atomic absorption. Conversion of energy to  $k$  space followed before  $k^3$  weighting of the data. The EXCURV98 code was then used to model the structure from the parameters of the radial shells of atoms surrounding the central atom. Phase shifts were calculated by *ab initio* curved wave theory methods in EXCURV98 for the central atom and for all backscattering elements in the samples. Multiple scattering effects were not considered, since only the nearest coordination shells are probed at these low energies. Such a simplification has already been employed for the study of non-stoichiometric apatites[44] and bioactive glasses[45] and bone[46] by K-edge EXAFS spectroscopy.

#### *Computational investigation of the site of incorporation of Mg*

The distribution of Mg in the hydroxyapatite lattice was investigated by a combination of electronic structure techniques and interatomic potential methods.[28-30, 47-50] It is noteworthy that both approaches have already been used to investigate ionic substitutions in apatite phases. Although interatomic potential methods are more efficient for dealing with structures containing a very large number of atoms, it is important first to validate a given method by comparing the results with electronic structure techniques.

The electronic structure calculations were performed using the SIESTA code [51], which employs Density Functional Theory [52], norm-conserving pseudopotentials and linear combinations of numerical atomic orbitals (LCAO) to calculate the total energy of the system. We have used the Perdew-Burke-Ernzerhof (PBE) [53] generalized gradients approximation (GGA) for the exchange-

correlation functional, whereas pseudopotentials for all atoms were generated in the Troullier-Martins manner [54]. The basis sets used for all atoms were of the DZP type (double  $\zeta$  with polarization), except for the oxygen and hydrogen in the hydroxy group, for which the basis sets were obtained from the optimization of water at 0.2 GPa [55, 56]. The unit-cell was optimized using a cutoff energy of 250 Ry, sampling was taken at the  $\Gamma$  point and a force tolerance of 0.01 eV/Å was used. The suitability of cutoff energy,  $k$  points and the force tolerance were evaluated by monitoring the convergence of the total energy with respect to the various parameters and validated against the structural properties of hydroxyapatite.

The larger-scale systems were modeled using the General Utility Lattice Program (GULP) [57-59], which uses interatomic potential simulation techniques based on the Born model of solids [60], which assumes that the ions in the crystal interact via long-range electrostatic forces and short-range forces, including both the repulsions and Van der Waals attractions between neighbouring electron charge clouds. The interatomic potential model for hydroxyapatite was taken from the work of de Leeuw [61], which includes electronic polarisability via the shell model of Dick and Overhauser [62]: each polarisable ion (in this case oxygen), is represented by a core and a massless shell, connected by a spring. The polarisability of the oxygen ions is then determined by the spring constant and the charges of the core and shell. When necessary, angle-dependent forces are included to allow directionality of bonding, for example in the covalent phosphate anion. In order to make geometry predictions, the lattice energies are minimized with respect to the structural parameters, until the forces acting on the ions are all less than 0.001 eV Å<sup>-1</sup>. All structures reported are the result of constant pressure energy minimizations, with an external pressure set to zero, where not only the ionic positions but also the cell parameters are allowed to vary to find the energy minimum.

The hexagonal crystal structure of hydroxyapatite has the  $P6_3/m$  space group [1, 63-65]. The 4e Wyckoff positions are occupied by two hydroxy oxygen atoms, each with 1/2 occupancy[65]. In order to translate this structure into a model with full occupancies for the hydroxy groups, as is required to carry out the calculations, we have assigned alternate 0 and 1 occupancies to these sites

along the hydroxy channels in the  $c$  direction, thus changing the space group of the hydroxyapatite unit cell from  $P6_3/m$  to  $P6_3$ . It is noteworthy that within the channels, the hydroxy groups were all oriented in the same direction to form OH...OH...OH chains, as this corresponds to the most stable configuration.[66, 67] However, since there is only one hydroxy channel per hexagonal unit cell, all the hydroxy groups in the periodic structure are oriented in the same direction, thereby creating a net electric polarisation per unit cell. In contrast, in the real structure, disorder in the relative orientation of the parallel OH channels means that electric polarisation is not present in the material. Therefore, in order to create a more realistic structure, the smallest cell in our simulations is doubled in the  $b$  direction, and the two OH channels of the resulting supercell were assigned opposite directions. The larger supercells used in our simulations are all multiples of this (1 x 2 x 1) simulation cell. It is noteworthy that the antiparallel orientation of the hydroxy groups in neighbouring columns, as shown in Figure 1, has been calculated to be slightly more stable than the parallel configuration [67] and it coincides with the arrangement of the hydroxy groups in pure, synthetic HA, which crystallises as an ordered monoclinic structure ( $P2_1/b$ ) with a double unit cell compared to the hexagonal structure [68, 69]. However, given that natural HA and the species synthesized here have the hexagonal structure, the (1 x 2 x 1) “hexagonal”-derived structure was used as a starting point for all our calculations on HA and Mg-HA, thus allowing direct comparison of the simulations with experimental data. Calculations were carried out on the (1 x 2 x 1) simulation cell (which has a total of 20 cation sites), and the (2 x 2 x 1) and (1 x 2 x 2) supercells (40 cation sites), for the investigation of the incorporation of Mg into the inequivalent Ca(I) and Ca(II) positions.

#### *DFT calculations of the NMR parameters*

NMR calculations were then performed on the various simulation cells described above, in order to determine the NMR parameters of all the nuclei present in Mg-HA. These first principles calculations based on the GIPAW method[70] were performed within Kohn-Sham DFT using the PARATEC code.[71] As previously, the crystalline structures were described as infinite periodic

systems using three-dimensional periodic boundary conditions. The PBE generalised gradient approximation was used and the valence electrons were described by norm conserving pseudopotentials[72] in the Kleinman-Bylander form.[73] The core definition for O and Mg is  $1s^2$  and it is  $1s^2 2s^2 2p^6$  for P and Ca. The core radii are 1.2 a.u. for H, 1.45 a.u. for Ca, 1.5 a.u. for O and 1.59 a.u. for Mg. The wave functions are expanded on a plane wave basis set with a kinetic energy cut-off of 80 Ry. The isotropic chemical shift  $\delta_{\text{iso}}$  is defined as  $\delta_{\text{iso}} = -[\sigma - \sigma^{\text{ref}}]$  where  $\sigma$  is the isotropic shielding and  $\sigma^{\text{ref}}$  is the isotropic shielding of the same nucleus in a reference system as previously described for  $^1\text{H}$ ,  $^{31}\text{P}$  and  $^{43}\text{Ca}$ . [37, 74] For  $\sigma^{\text{ref}}(^{25}\text{Mg})$ , external referencing with respect to crystalline MgO[75] was chosen, with  $\delta_{\text{iso}}(^{25}\text{Mg}) = 26.3$  ppm.[76] For  $^1\text{H}$ ,  $^{31}\text{P}$ ,  $^{43}\text{Ca}$  and  $^{25}\text{Mg}$ , the values of isotropic chemical shifts were calculated. In addition, in the case of  $^{43}\text{Ca}$  and  $^{25}\text{Mg}$ , the quadrupolar parameters  $C_Q$  and  $\eta$  were also analysed.[38] It should be noted that based on previous studies and our own experience, the error on calculated  $^1\text{H}$  and  $^{31}\text{P}$  isotropic chemical shifts is estimated at  $\sim 0.4$ [77] and 0.7 ppm,[78] respectively, whereas it is  $\sim 3$  to 5 ppm on  $^{43}\text{Ca}$  and  $^{25}\text{Mg}$  isotropic chemical shifts, and  $\sim 0.5$  to 2 MHz on  $^{43}\text{Ca}$  and  $^{25}\text{Mg}$   $C_Q$  values,[37, 39] respectively.

## Results and discussion

### 1. Experimental study of Mg-HA

#### 1a. Description of the local environment of the ions in HA

There are two crystallographically different calcium sites in the HA unit cell: Ca(I) and Ca(II). The four Ca(I) ions in the unit cell are usually referred to as “columnar calcium sites”, because they form single atomic columns perpendicular to the basal plane. On the other hand, the six Ca(II) ions in the unit cell are arranged in triangles around the hydroxy groups (OH), thereby forming hexagonal channels along the *c*-direction of the structure.

As illustrated in Figure 2, the local environment of calcium in the two sites is very different. Each Ca(I) is coordinated to nine O atoms belonging to six different  $\text{PO}_4^{3-}$  anions; six of these oxygens are located at less than 2.55 Å from the cation, whereas the three others are more distant. Ca(II) cations have a less regular seven-fold coordination: they are bound to six O atoms belonging to five different phosphates, and to one hydroxy group. When the local environment of the anions is considered, it appears that  $\text{PO}_4^{3-}$  tetrahedra have five Ca(II) and four Ca(I) sites in their vicinity, in contrast with the hydroxy groups which are only surrounded by Ca(II) sites.

In order to learn how the incorporation of a small cation like  $\text{Mg}^{2+}$  in the HA lattice can affect the cation and anion environments, solid state NMR and X-ray absorption spectroscopy studies were carried out. Given that previous reports have shown that it is preferable to keep the Mg concentration low in order to avoid losing the crystallinity of the HA lattice and forming more amorphous phases,[13] we prepared a Mg-HA containing ~10% Mg (Mg10-HA). SEM, TEM, and XRD confirm the crystallinity of this sample and the presence of Mg in the HA lattice (Figure S1). Elemental analyses show that the actual amount of Mg in the lattice is ~9%, which is slightly less than the ionic concentrations initially introduced in solution, meaning that the actual formula for Mg10-HA is  $\text{Ca}_{9.1}\text{Mg}_{0.9}(\text{PO}_4)_6(\text{OH})_2$ . The observation of a lower Mg content in the solid is not entirely surprising, given previous reports on Mg-HA phases prepared according to similar synthetic procedures.[13]

### 1b. NMR analysis of the local environment of the anions

The  $^1\text{H}$  MAS NMR spectrum of Mg10-HA is shown in Figure 3a. Two main signals are observed, one narrow one at 0 ppm, which corresponds to the hydroxy, and the other at  $\sim 5.3$  ppm, which can be assigned to water molecules mainly located at the surface of HA crystallites.[79] The position of the hydroxy peak is the same as for non-substituted HA, but the signal is slightly broader (increase of the full-width at half maximum by 0.4 ppm), which suggests that there is a larger distribution of environments around the hydroxy. This change in environment around the hydroxy ion could be due to the presence of some Mg cations having entered the neighbouring Ca(II) site, and to the structural distortions caused by the incorporation of Mg and the contraction of the HA unit cell, which could induce changes in the O-H bond distances.

The  $^{31}\text{P}$  MAS solid state NMR spectrum of Mg10-HA is shown in Figure 3b. Only one asymmetric peak is observed. Its maximum is slightly shifted compared to non-substituted HA (2.6 ppm vs 2.8 ppm),[80] and the signal is  $\sim 1$  ppm broader at half maximum, with a tailing towards high frequencies. These observations show that there is a larger variety of environments around the phosphates in Mg-HA, which can be due to the presence of  $\text{Mg}^{2+}$  cations occupying different neighbouring positions (see Figure 2), and also to the structural distortions of the HA lattice which can induce slight rotations of the phosphate groups and small variations in the P-O bond distances and O-P-O bond angles.[38, 81]

The only clear conclusion which can be drawn at this stage from these  $^1\text{H}$  and  $^{31}\text{P}$  NMR spectra of Mg10-HA is that the incorporation of Mg in HA creates a larger variety of environments around the phosphate and hydroxy anions. Thus, in contrast with some previous studies, in which shifts and changes in the  $^1\text{H}$  or  $^{31}\text{P}$  signals could be used as indicators of the preferential location of substitutional cations like  $\text{Pb}^{2+}$  in HA lattices,[26, 82] the very low level of incorporation of Mg and the distortions it creates in the HA structure makes it difficult here to derive any further information.



### 1c. Analysis of the local environment of the calcium

Analyzing the local environment of calcium in non-crystalline and disordered materials is particularly challenging. Indeed,  $\text{Ca}^{2+}$  is a metal cation with closed electron shells, which makes it silent to spectroscopies like EPR or UV-Vis. Furthermore, the NMR-active isotope,  $^{43}\text{Ca}$ , is a spin-7/2 low- $\gamma$  nucleus (i.e. with a small magnetic moment) of low natural abundance ( $< 0.14\%$ ), [38, 83] which makes it particularly difficult to study by NMR. Nevertheless, we have recently shown that natural abundance  $^{43}\text{Ca}$  solid state NMR is well adapted to the study of apatite phases. [26, 34, 46] Indeed, the two calcium sites of HA are resolved at high magnetic fields, with the high frequency peak corresponding to the Ca(II) site.

The  $^{43}\text{Ca}$  NMR spectrum of Mg10-HA (Figure 4) shows that the relative intensity of the Ca(II) peak decreases compared to HA, suggesting that Mg has preferentially entered this site. This simple interpretation of the  $^{43}\text{Ca}$  NMR spectrum of Mg10-HA must, however, be considered carefully. Indeed, it relies on the assumption that the  $^{43}\text{Ca}$  parameters of each site remain the same in the Mg-substituted species. Given that in calcium-oxoanion species the  $^{43}\text{Ca}$  isotropic chemical shifts mainly depend on the average  $\text{Ca}\cdots\text{O}$  bond distance around calcium, this means that the average environment of calcium and average  $\text{Ca}\cdots\text{O}$  bond distances in each site must be very similar to those of non-substituted HA, for this conclusion to remain valid. [37, 84, 85] In order to investigate this point, the local environment of calcium was analyzed using X-ray absorption spectroscopy, because Ca K-edge XANES (X-ray absorption near edge structure) can provide information about the local geometry around calcium, [86] and Ca K-edge EXAFS (Extended X-ray absorption fine structure) on the average  $\text{Ca}\cdots\text{O}$  bond distance in the first sphere. [46]

As shown in Figure 5, the Ca K-edge XANES spectrum of Mg10-HA is nearly identical to the one of non-substituted HA, especially in the region of the pre-edge, which is sensitive to the local distortion around calcium sites. On the other hand, as shown in Figure 6, the experimental EXAFS

spectra  $k^3\chi(k)$  and the moduli of the Fourier Transforms (FT) of HA and Mg10-HA are also very similar. For both compounds, the first two Ca $\cdots$ O shells ( $< 3 \text{ \AA}$ )[46, 87] appear to be nearly identical, the maximum intensity on the FT spectra being reached at the same distance. This suggests that the average bond distance between calcium and its nearest oxygen neighbours is very similar for both samples.

However, it is noteworthy that the intensity of the FT signal corresponding to the more distant shells ( $> 3 \text{ \AA}$ ) is slightly smaller in the case of Mg10-HA (shadowed region in Figure 6). Given that for HA this part of the spectrum arises from the scattering of more distant oxygen, phosphorus and calcium atoms,[46, 87] the decrease in intensity could be caused by the presence of magnesium neighbours, which are lighter and thus weaker back-scatterers than calcium. Alternatively, the decrease could also reflect a loss of long-range ordering around calcium, because of the structural distortions of the HA lattice caused by the incorporation of Mg.[46] In any case, it was found that this decrease cannot be used to determine the preferential location of Mg, because fits of similar quality were obtained when considering its incorporation into one site or the other (see Table S1 in the supplementary materials).

All in all, from these X-ray Absorption Spectroscopy analyses, it is clear that the introduction of low levels of Mg in the HA phase does not significantly modify the local geometry and average Ca $\cdots$ O bond distance around the cation. Hence, the  $^{43}\text{Ca}$  NMR data suggest that the preferential site of incorporation of Mg is indeed the Ca(II) site.

#### **1d. Towards the analysis of the local environment of the magnesium**

Determining the local environment of magnesium in non-crystalline or disordered materials is particularly challenging. Indeed, just like calcium,  $\text{Mg}^{2+}$  is a closed shell diamagnetic cation, and magnesium-25, the NMR active isotope, is a spin-5/2 low- $\gamma$  nucleus of low natural abundance ( $\sim 10.0\%$ ),[38] with a relatively large quadrupole moment, meaning that the NMR signals can be very broad. Although techniques like  $^{25}\text{Mg}$  solid state NMR[38, 39, 76, 88] and Mg K-edge EXAFS and

XANES[89-91] are being developed to help investigate the local structure around magnesium, they cannot be used routinely, because they require access to ultra-high field magnets or soft X-ray synchrotron sources. Furthermore, these experiments can be very time-consuming, especially for samples in which the Mg content is low.

A first attempt to analyse directly the local environment of Mg in Mg10-HA was nevertheless performed, by recording its  $^{25}\text{Mg}$  MAS NMR spectrum at natural abundance at 19.6 T (Figure 7). Despite the use of a large volume rotor, the signal is still weak after ~20h of acquisition. The lineshape is complex, with a narrow feature and a broad underlying component. Such a spectrum, on its own, does not allow definitive conclusions about the local structure around magnesium in the sample: it would be necessary here to record high field fast MAS spectra of a  $^{25}\text{Mg}$  labeled sample to gain more information on the different components and determine the actual ratio between the different types of environments. Nevertheless, the spectrum observed here shows that there are several different local environments around Mg in the sample analysed, leading to a variety of  $^{25}\text{Mg}$  quadrupolar coupling constants, and thus to complex  $^{25}\text{Mg}$ -NMR spectra.

Overall, the experimental data reported in this section brings new information about the structure of Mg-HA: *(i)* Mg preferentially enters the Ca(II) site, *(ii)* there are distributions in the local structure around the phosphate and hydroxy anions, *(iii)* the average Ca...O bond distance in the first sphere and local geometry around calcium appear to be hardly affected by the presence of low levels of Mg in the lattice, and *(iv)* several different Mg local environments are found in the crystallites, which could be due to small changes in Mg...O bond distances. Given the lack of an experimental crystal structure for Mg-substituted HA, the purpose of the next section is to use a computational approach to model Mg-HA phases, in order to account for the preferential location of Mg in the Ca(II) position, to understand better the NMR data, and to gain direct insight on the structural changes of the HA lattice and substitution mechanism of Mg.

## 2. Computational study of Mg-HA

### 2a. Modeling Mg-HA structures

#### 2.a.a. DFT modelling of 5% Mg substitution in HA

Extensive calculations were carried out using different computational methods and simulation cells, as described in the computational methods section, in order to derive sound conclusions on the incorporation of Mg in HA. Using *DFT calculations*, the structure of a (1 x 2 x 1) supercell of pure hydroxyapatite (of general formula  $\text{Ca}_{20}(\text{PO}_4)_{12}(\text{OH})_4$ ) was first relaxed, by allowing both the lattice vectors and the positions of the ions to vary. The cell parameters for this relaxed HA were  $a = 9.40 \text{ \AA}$ ,  $b = 18.81 \text{ \AA}$ , and  $c = 6.95 \text{ \AA}$ , which is in very good agreement with the experimental data (discrepancy <1.0 %), with only a slight expansion in the  $c$ -direction. We then considered the substitution of an isolated Mg cation in this (1 x 2 x 1) supercell, which leads to a Mg concentration of 5 mol %. According to the symmetry of this cell, there are three types of Ca(II) sites (Ca(IIa), Ca(IIb) and Ca(IIc)) and two types of Ca(I) sites (Ca(Ia) and Ca(Ib)), which differ slightly in the distances to the neighbouring O atoms. The calculated energies showed a preference for Mg to be incorporated into the HA structure at Ca(II) positions (see Table 1), in agreement with the  $^{43}\text{Ca}$  solid state NMR analyses. Interestingly, it appears that the incorporation of Mg in the Ca(IIa) site leads to a larger energy difference (~0.14 eV) with the Ca(I) configurations, than its incorporation in the Ca(IIb) and Ca(IIc) sites, for which the energy difference is reduced to 0.04 and 0.01 eV, respectively. It should be noted that a similar observation had been reported previously in a computational investigation of the incorporation of lead in HA,[50] where the presence of energetically inequivalent Ca(I) positions had been noted. Overall, this finding underscores the requirement that *all* the different possible configurations relating to the incorporation of a cation like  $\text{Mg}^{2+}$  in one or the other site must be taken into consideration before concluding on its preferential location in the lattice.

Structural changes are observed as Mg enters the (1 x 2 x 1) lattice. First, it appears that the cell volume decreases, in agreement with experimental XRD observations.[13, 20, 22, 92] Such a

contraction reflects a decrease in the lattice parameters, due to the presence of small  $\text{Mg}^{2+}$  cations. It is noteworthy that previous computational studies of Mg-HA could not account for this contraction, because calculations had been carried out considering that the HA cell shape and cell dimensions remained unchanged after incorporation of Mg.[28] Calculations show that there are differences in the cell dimensions according to whether Mg enters the Ca(I) or Ca(II) site: (i) the overall reduction in volume of the cell here is slightly larger when Mg is in the Ca(I) position ( $\sim 1.2\%$  decrease), and (ii) the  $c$  lattice parameter does not seem to decrease when Mg is in the Ca(II) site. The latter observation could appear to be in conflict with previous experimental studies, which show a decrease in the  $c$  parameter of  $\sim 0.01$  to  $0.02$  Å for  $\sim 5\%$  Mg substitution.[21, 31] However, it is more likely that this discrepancy reflects the limits of the calculations for such low levels of Mg.

A closer analysis of the *local* environment of  $\text{Mg}^{2+}$  in the (1 x 2 x 1) cells provides further insight as to how the lattice accommodates the presence of this substituent. The co-ordination distances around Mg in the Ca(I) site show a reduction of  $\sim 0.3$  Å of six  $\text{Mg}\cdots\text{OPO}_3$  distances compared to  $\text{Ca}\cdots\text{OPO}_3$ , and an increase of the three other  $\text{Mg}\cdots\text{OPO}_3$  distances by  $\sim 0.4$  Å (see Table S2 in SI). When Mg is incorporated in the Ca(II) site, the changes in local environment of the cation are less significant: the three shorter  $\text{Mg}\cdots\text{OPO}_3$  distances are reduced by  $\sim 0.25$  Å compared to  $\text{Ca}\cdots\text{OPO}_3$ , the  $\text{Mg}\cdots\text{OH}$  distance is reduced by  $\sim 0.3$  Å, but the remaining  $\text{Mg}\cdots\text{OPO}_3$  distances only increase by less than  $0.1$  Å (see Figure S2 and Table S3 in SI). In this case, the substituting Mg moves away from the crystallographic Ca(II) position, thereby slightly distorting the hydroxy channel, and reducing its distance to the two Ca atoms of the Mg-Ca(II)-Ca(II) triangle.

Concerning the local structure around the other ions present in the (1 x 2 x 1) cell, it is clear that the presence of Mg leads to a larger variety of environments compared to the non-substituted structure. In the case of the phosphate and hydroxy ions, this is mainly related to the presence of  $\text{Mg}\cdots\text{OPO}_3$  and  $\text{Mg}\cdots\text{OH}$  interactions, which induce changes in the average  $\text{M}\cdots\text{O}$  distances ( $\text{M} = \text{Ca}, \text{Mg}$ ) and small rotations of these anions. In the case of calcium, although a larger distribution of local environments is also observed, we note that on average, the distances around the Ca(I) and Ca(II) sites

vary by less than 0.01 Å after Mg-incorporation (see Table S4 in SI), which is consistent with the observations made using Ca K-edge XANES and EXAFS (*vide supra*).

Overall, this initial DFT analysis of a (1 x 2 x 1) substituted HA structure with 5% Mg shows that the incorporation of the cation in the Ca(II) site is energetically more favourable, and that the presence of Mg induces changes in cell dimensions and local environments of the different ions, in agreement with experimental observations. This site preference could perhaps stem from the fact that when Mg enters the Ca(II) position, the local changes in M···O distances around the cations seem less significant than when it enters the Ca(I) site and thus more favourable energetically for the structure as a whole. However, it may be important to learn whether this trend is maintained for higher levels of Mg (notably for more substituted species as in Mg-HA10), and to investigate whether there can be any clustering and/or domain formation of the Mg<sup>2+</sup> cations when they enter the HA lattice.

#### *2.a.b. Force field modelling of higher levels of Mg substitution in HA*

In order to study a 10% substituted Mg-HA, 2 Mg cations need to be incorporated in the (1 x 2 x 1) supercell. As shown above, all the possible configurations related to the incorporation of the cation in the Ca(I) and Ca(II) positions must be considered. The “Site Occupancy Disorder” program (SOD)[93] was therefore used to create the complete configurational space and to extract the subspace of the symmetrically inequivalent configurations. In this case, 55 inequivalent configurations were generated for Mg<sub>2</sub>Ca<sub>18</sub>(PO<sub>4</sub>)<sub>12</sub>(OH)<sub>4</sub>, which means that it would be computationally prohibitive to analyze by DFT. Thus, an alternative method based on interatomic potentials was used.

First, this interatomic approach was validated by comparing the results of the interatomic potential-based calculations with DFT, on the singly-substituted (1 x 2 x 1) cell (equivalent to 5% substitution). Similar geometric and energetic trends were observed with this model. Indeed, the Mg cations showed an overall preference to be incorporated in the Ca(II) site (see Table S5 in SI). In addition, there is a general decrease in cell volume, and the co-ordination distances around a Mg

cation in the Ca(II) position once again display a clear shortening of the  $M\cdots OH$  distance and of three  $Mg\cdots OPO_3$  distances (see Table S3).

The solid solution with two Mg cations in the (1 x 2 x 1) supercell was then considered, which is equivalent to a 10% substitution with the general formula for these phases of  $Mg_2Ca_{18}(PO_4)_{12}(OH)_4$ . Out of the 55 inequivalent configurations, Mg displayed a clear preference for the Ca(II) sites. In this case, it is noteworthy that a  $\sim 0.9\%$  decrease in the  $c$  parameter of the lattice was now observed, in agreement with experimental data. The arrangement of the Mg atoms around the OH column for the structure with the lowest energy is shown in Figure 8. The two Mg ions are located in Ca(II) positions of the same hydroxy channel, but at the opposite vertices of triangles around two neighbouring OH groups. This suggests that Mg substituents will tend to aggregate locally within the HA structure.

Having first studied the (1 x 2 x 1) simulation cell, we next proceeded to simulate other Mg compositions using the larger (1 x 2 x 2) and (2 x 2 x 1) supercells in order to better understand the site preference and the clustering of Mg substituents in the HA lattice, and also to avoid any possible computational artifacts which can result from the interaction between defects in small simulation cells. Given that the general formula of these supercells is  $Ca_{40}(PO_4)_{24}(OH)_8$ , the presence of 40 cations obviously generates a much greater number of inequivalent configurations. Thus, it became computationally prohibitively expensive to run geometry optimizations for substituted structures containing more than four Mg cations in these supercells. Indeed, five inequivalent configurations were investigated for a single substituting Mg, whereas 105 configurations were identified for two Mg, 1235 configurations for three Mg, and 11500 configurations for four Mg, with the corresponding Mg concentrations for these structures of 2.5 mol %, 5 mol %, 7.5 mol %, and 10 mol % respectively. The very large number of configurations for 10% substitution meant that these could not be investigated using SOD, and in order to simulate some of the possible structures with 10% Mg, we have used the most stable configuration at 7.5% Mg as a starting structure to simulate the possible configurations with an additional Mg in the supercell.

For all these supercells, a preferential incorporation of magnesium cations in the Ca(II) site was again observed. This is well illustrated in Figure 9, which shows the difference in energy for all the configurations with Mg substitutions in Ca(II) sites only, in both Ca(II) and Ca(I) sites, and in Ca(I) sites only of the (1 x 2 x 2) supercell. In all cases, the energy difference between Mg(II) sites only and mixed Mg(II) and Mg(I) sites was found to be ~0.25 eV in favour of Mg(II) only, which confirms the higher stability of structures with Mg in Ca(II)-type environments over a larger range of composition. Interestingly, as in the smaller (1 x 2 x 1) supercell, it appears that, as the Mg concentration increases, the most stable configurations are again those where Mg ions are located at alternating vertices of different triangles around the hydroxy groups of one channel, and that the Mg...OH distances are once more strongly reduced compared to the Ca...OH (see Table S6 and Figure S3). It is noteworthy that such structural features, which could have consequences for the reactivity of Mg-HA phases, would have been very challenging to investigate experimentally and computation has thus proven itself to be an extremely useful complementary technique for these studies.

## 2b. Computation of the NMR parameters of Mg-HA structures

Having gained information on the structural features of Mg-HA, the  $^1\text{H}$ ,  $^{31}\text{P}$ ,  $^{43}\text{Ca}$  and  $^{25}\text{Mg}$  NMR parameters of different optimized supercells were then calculated and compared to the data reported in section 1, in order to try to further interpret the experimental NMR data. Table 2 summarizes the results obtained on the (1 x 2 x 1) cell optimized using DFT, and on the (1 x 2 x 2) cell optimized using interatomic potentials. In the latter case, only the lowest energy structures with one Mg in the Ca(I) or Ca(II) position were considered. It is noteworthy that given the large number of inequivalent phosphate, hydroxy and calcium environments in the cell, average values have been reported, together with the associated standard deviation.

The calculated  $^1\text{H}$  and  $^{31}\text{P}$  chemical shifts are in agreement with the experimental spectrum. Indeed, on average, the  $\delta_{\text{iso}}$  values shift by less than 0.6 ppm with respect to the non-substituted



structure, whereas the standard deviation increases, thereby reflecting the increase in linewidth of the OH and phosphate signals on the  $^1\text{H}$  and  $^{31}\text{P}$  NMR spectra of Mg10-HA. It is worth noting that the shift in  $\delta_{\text{iso}}(^1\text{H})$  is actually always slightly smaller when Mg is incorporated in a Ca(II) position, meaning that  $^1\text{H}$  NMR could act as additional experimental evidence of the preferential substitution into the Ca(II) site.

The calculated  $^{43}\text{Ca}$  NMR parameters of the substituted species reveal that the average  $\delta_{\text{iso}}$  values for Ca(I) and Ca(II) sites stay fairly similar to those in the non-substituted samples, which is consistent with the fact that the average Ca(I)···O and Ca(II)···O distances have not been significantly altered by the incorporation of Mg, as indicated above (see Tables S1 and S4). In addition, this proves definitively that our interpretation of the  $^{43}\text{Ca}$  NMR spectrum of Mg10-HA was indeed accurate, because the two calcium sites will remain sufficiently distinct to be resolved at 18.8 T. It is worth noting that calculations also show that there is a larger distribution in Ca(I) and Ca(II) environments compared to the non-substituted samples, as reflected in the increase in the standard deviations of  $\delta_{\text{iso}}(^{43}\text{Ca})$ ,  $C_Q$  and  $\eta$ .

The comparison of the calculated  $^{25}\text{Mg}$  NMR parameters is particularly interesting. Indeed, it appears that very different values of  $\delta_{\text{iso}}(^{25}\text{Mg})$ ,  $C_Q$  and  $\eta$  are obtained, according to which site Mg has entered and which Mg-HA structure is considered. In particular, absolute  $C_Q$  values ranging between 8.6 and 12.0 MHz were found for Mg entering Ca(II) sites, and between 5.4 and 7.5 MHz for Ca(I) sites, which could be one of the reasons for the complicated  $^{25}\text{Mg}$  NMR spectrum obtained. Indeed, it appears that  $^{25}\text{Mg}$  NMR parameters are very sensitive to the local environment of Mg, and that even if Mg enters exclusively the Mg(II) position, very small deviations in Mg···O bond distances, like those reported in Tables S3 and S6, might entail strong changes in  $C_Q$  values and thus in NMR linewidths. As a result, the presence of both large and narrower components of the spectrum could simply reflect the distribution in Mg local environments and therefore in  $^{25}\text{Mg}$   $C_Q$  values in the structure. NMR computations are thus particularly useful understanding fully the experimental data for biomaterials like Mg-HA.

## Conclusion

The mechanism of incorporation of Mg in HA was studied using a combined experimental-computational approach.  $^{43}\text{Ca}$  solid state NMR and Ca K-edge XAS experiments bring evidence of the preferential incorporation of Mg in the Ca(II) site, which is consistent with both DFT and force field calculations of Mg-HA structures containing up to 10% Mg, because the incorporation of the cation in the Ca(II) position is found to be energetically more favourable. From the computational data, information on the structure of Mg-HA was obtained. Deformations of the HA lattice mainly occur around the Mg, because the Mg $\cdots$ O bonds are much shorter than Ca $\cdots$ O ones. These structural changes lead to a larger variety of environments for the phosphate and hydroxy anions, in agreement with the experimental  $^1\text{H}$  and  $^{31}\text{P}$  solid state NMR data. More interestingly, the calculations show that when increasing the Mg content in the HA lattice, there is a preference for an ordered pattern of Mg ions in alternating positions of the Ca(II) triangles along a single OH channel. This suggests that in Mg-HA phases, Mg cations are not randomly distributed between the Ca(II) sites of lattice, but more probably segregated in small sections of higher content. These structural features are likely to have a direct impact on the properties of Mg-HA. Indeed, the preferential incorporation in the Ca(II) position might affect the reactivity of the hydroxy groups and thereby alter the biological responses of the substituted HA. In addition, the local clustering of Mg within the lattice could favour localized Mg-stimulated biological responses. Nevertheless, further computational and experimental investigations need to be carried out on apatite compositions more similar to those found in bone, to see how the presence of other substituents, notably carbonates, might further alter the structure of these phases. For such substituted-HA phases, the combination of experiments like multinuclear solid state NMR, computer simulations, *and* calculations of the NMR parameters of the different nuclei should also be used as a guideline to help understand their structure and properties.

## Acknowledgements

This work was supported by CNRS, BBSRC, EPSRC, the University of Warwick, University College London, the Royal Society for an international collaboration grant and Science City Advanced Materials project: Creating and Characterising Next generation Advanced Materials with support from Advantage West Midlands (AWM), and part funded by the European Regional Development Fund (ERDF). DL would like to thank the 6<sup>th</sup> European Community Framework Program for a Marie Curie IEF, and AW NSERC for a Canadian PDF. NAB and NHdL are grateful to EPSRC for a PhD+ award and acknowledge computer resources on the UK High Performance Computing Facility HECToR, which were provided via our membership of the UK's HPC Materials Chemistry Consortium (grant no. EPSRC EP/D504872). JCK was supported in part by WCU Program through the National Research Foundation of Korea (NRF) funded by the Ministry of Education, Science and Technology (No. R31-10069). NMR calculations were performed on the IDRIS supercomputer centre of the CNRS (Project 091461). ELETTRA (proposal 2007512) and the European Community (EU contract RII3-CT-2004-506008 - IA-SFS) are acknowledged for financial support Dr Andrea Cognigni and Dr Luca Olivi are thanked for their help on the XAFS beamline, and Dr Dong Qiu and Dr David Pickup for their assistance with XAS data. The NHMFL in Tallahassee is acknowledged for experimental time on the high field 19.6 T NMR magnet. Prof. Ray Dupree (University of Warwick, UK), as well as Prof. Hélène Pernot, Dr Guylène Costentin and Dr Jean-Marc Krafft (Université Pierre et Marie Curie, France) are thanked for fruitful discussions on this work.

**Supplementary Data** (see attached file)

*Figure S1*: SEM, TEM, XRD analyses of Mg10-HA; *Table S1*: Fitting parameters of the Ca K-edge EXAFS spectra of HA and Mg10-HA; *Table S2*: Coordination distances around Ca(I) and Mg(I) sites, in the (1 x 2 x 1) cell (as determined by DFT). *Figure S2*: Representation of the Mg environment when incorporated in the Ca(II) site in the (1 x 2 x 1) HA supercell optimized by DFT; *Table S3*.

Coordination distances around Ca(I) and Mg(I) sites, in the (1 x 2 x 1) cell; *Table S4*: Average coordination distances around all the Ca(I) and Ca(II) sites, in the (1 x 2 x 1) cell optimized using DFT; *Table S5*: Unit cell parameters of un-substituted and singly substituted HA in (1 x 2 x 1) supercell, as derived from interatomic potential calculations; *Table S6*: Co-ordination distances around four different Mg(II) sites in the most stable configuration of a 7.5% substituted (1 x 2 x 2) HA supercell. *Figure S3*: Representation of the most stable Mg arrangement in a (1 x 2 x 2) HA supercell substituted by a) 2.5 mol % Mg, b) 5 mol % Mg, c) 7.5 mol % Mg, and d) 10 mol % Mg.

## Figure captions

**Figure 1.** Representation of the hydroxyapatite structure perpendicular to the crystallographic  $c$  and  $a$  axes, showing the  $\text{OH}^-$  channels and the different types of Ca ions (Ca = green, O = red, P = purple, H = white).

**Figure 2.** Representation of the local environment of the cations and anions in HA, with indications on the co-ordination distances (in Å) around each ion[63] (Ca = green, O = red, P = purple, H = white).

**Figure 3.**  $^1\text{H}$  and  $^{31}\text{P}$  MAS-NMR spectra of Mg10-HA, recorded at 7.1 T.

**Figure 4.** Natural abundance  $^{43}\text{Ca}$  MAS NMR spectra of HA and Mg10-HA, recorded at 18.8 T.

**Figure 5.** Ca K-edge XANES spectra of HA and Mg10-HA.

**Figure 6.** Ca K-edge EXAFS and moduli of the Fourier transforms of HA and Mg10-HA. Details on the fits can be found in Supplementary Table S1.

**Figure 7.** Natural abundance  $^{25}\text{Mg}$  MAS NMR spectrum of Mg10-HA, recorded at 19.6 T. The asterisk corresponds to a spinning sideband.

**Figure 8.** Representation of the most stable Mg arrangement in the doubly-substituted (1 x 2 x 1) cell (Ca = green, Mg = gray, O = red, P = purple, H = white), with indications of the co-ordination distances (in Å).

**Figure 9.** Representation of the energy difference (in eV) between the most stable MgHA and the rest of the configurations in the (1 x 2 x 2) supercell substituted by a) 5 mol % Mg, b) 7.5 mol % Mg, and c) 10 mol % Mg.

## Figures

Figure 1

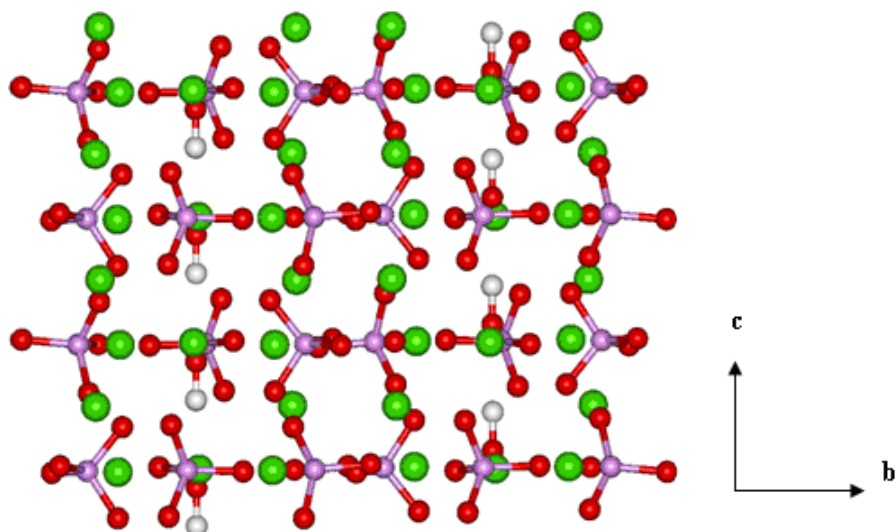
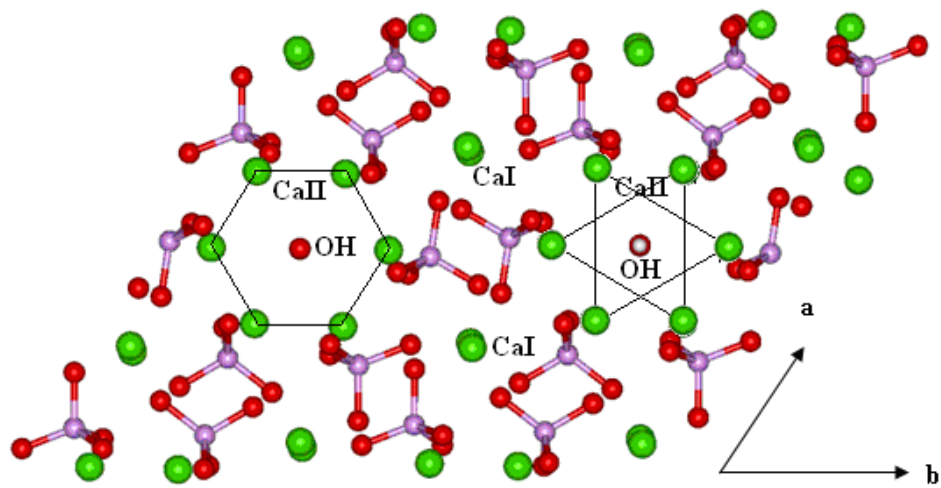
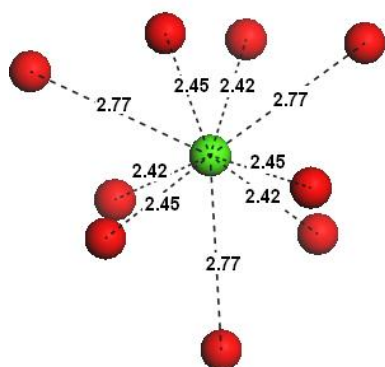


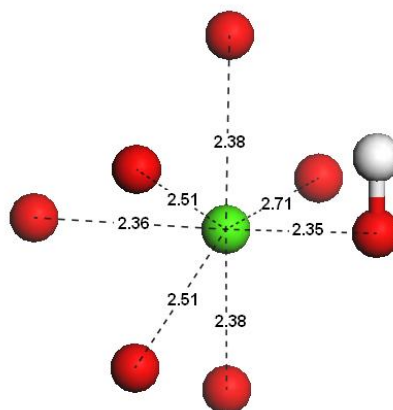
Figure 2

Cationic environments

Ca(I) site

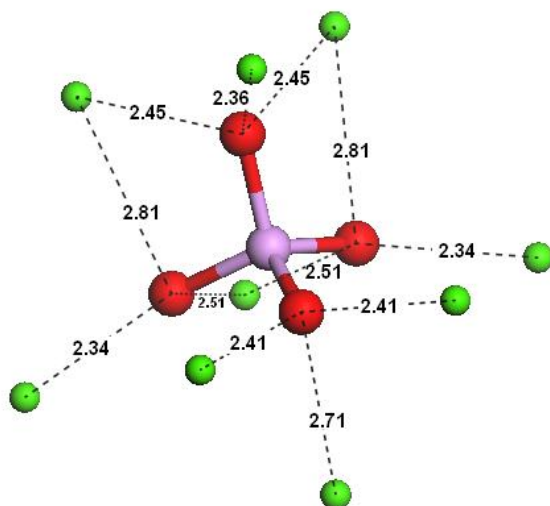


Ca(II) site



Anionic environments

$\text{PO}_4^{3-}$



$\text{OH}^-$  column

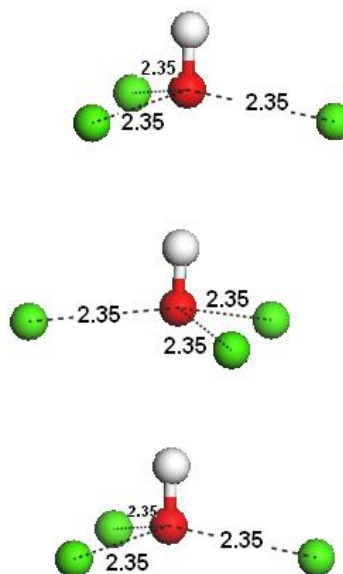


**Figure 3**

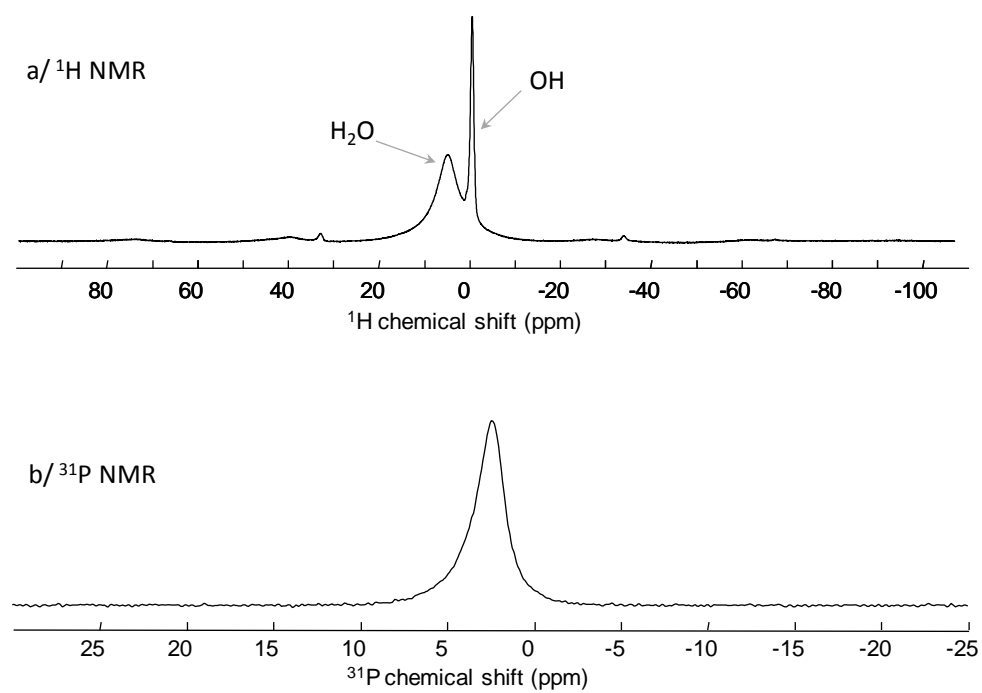




**Figure 4**

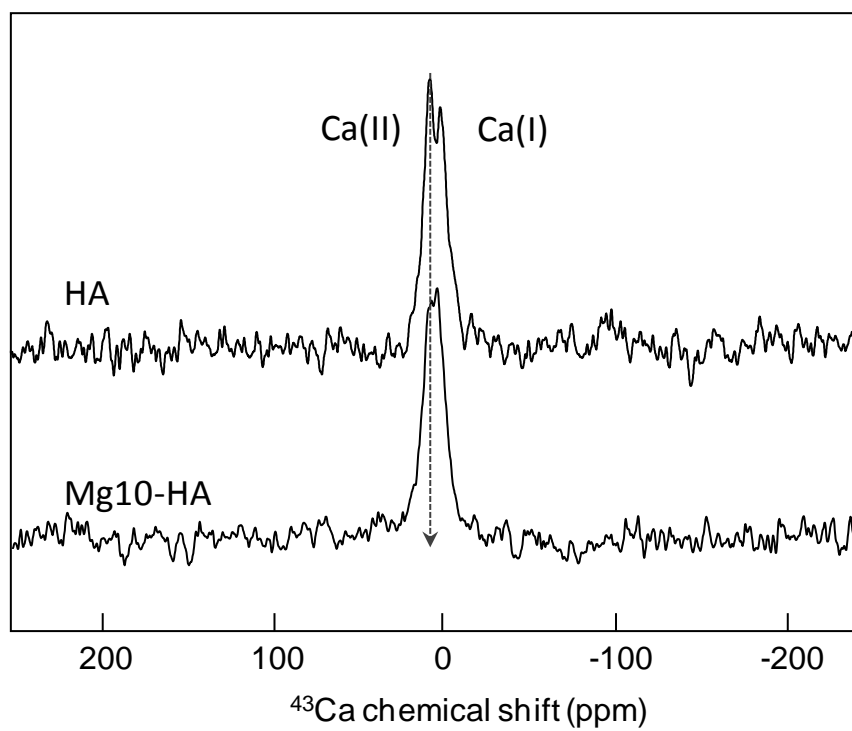


**Figure 5**

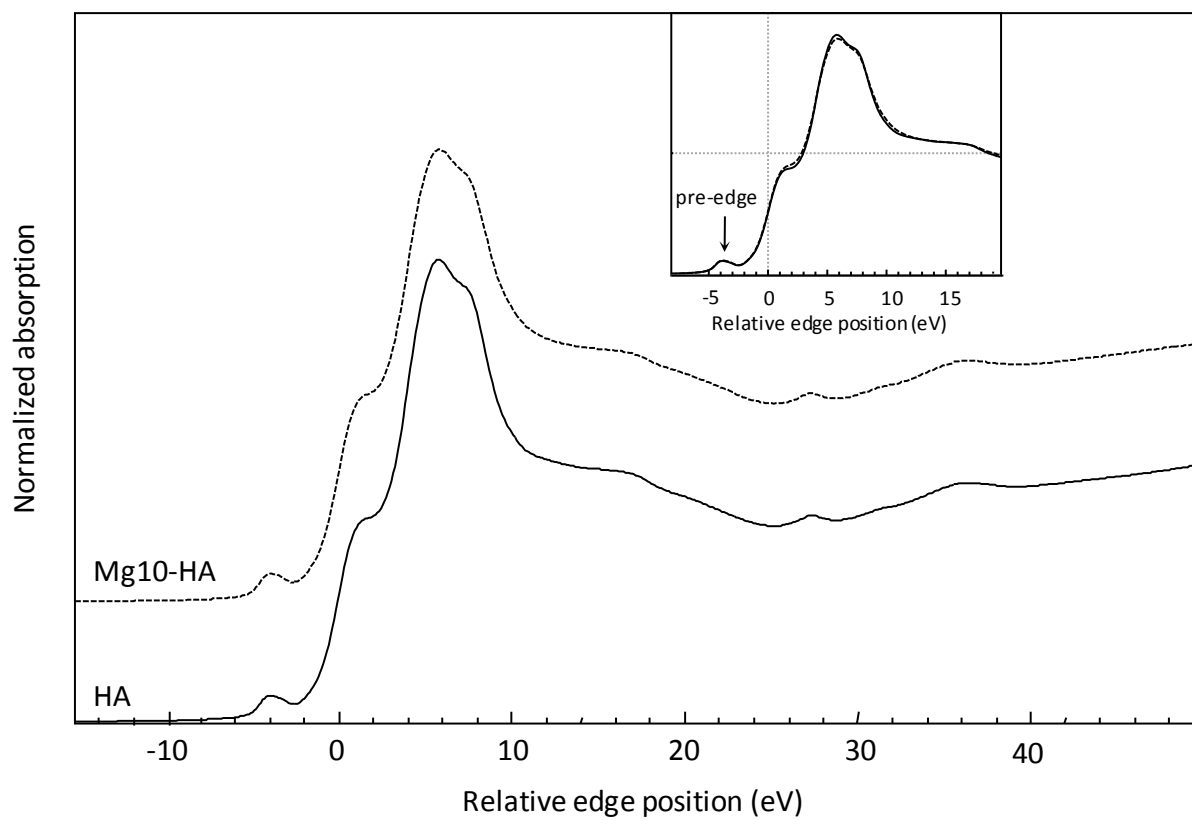


**Figure 6**

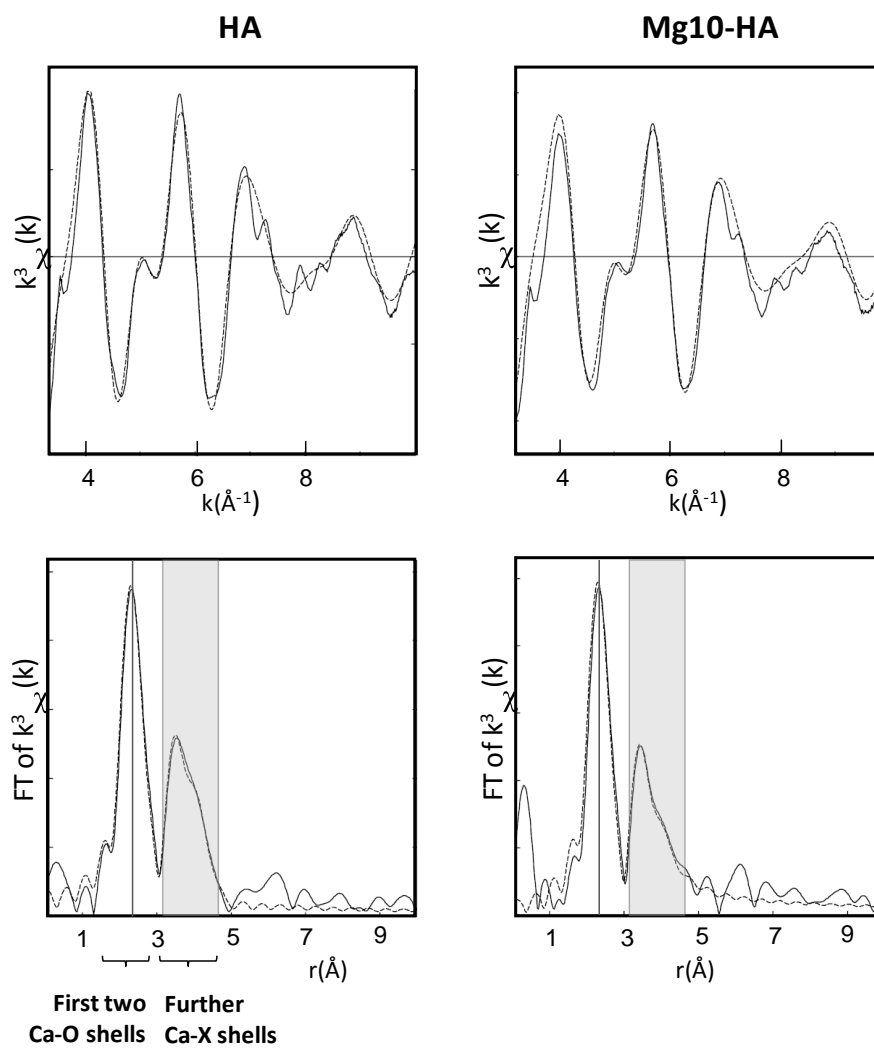


**Figure 7**

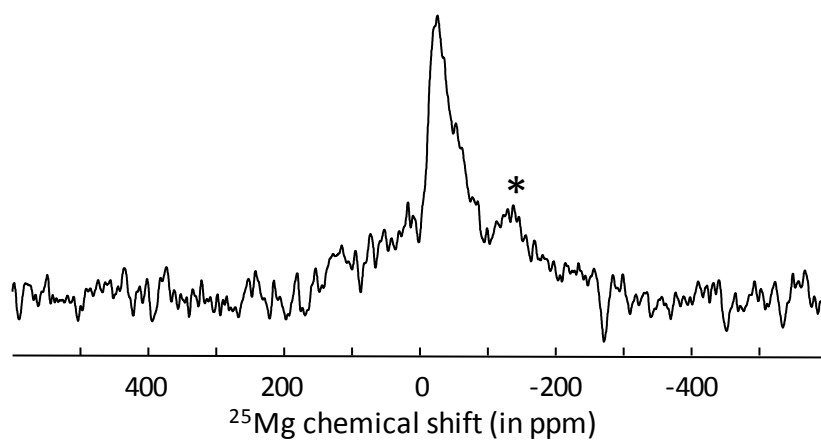


Figure 8

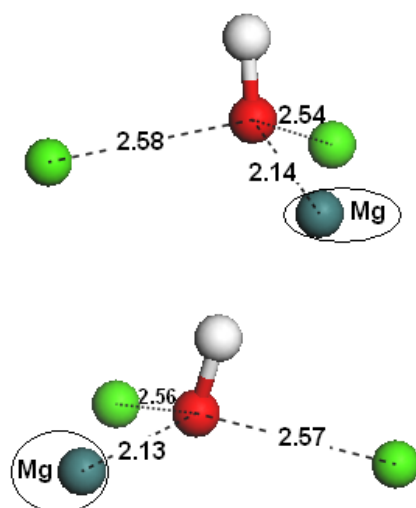
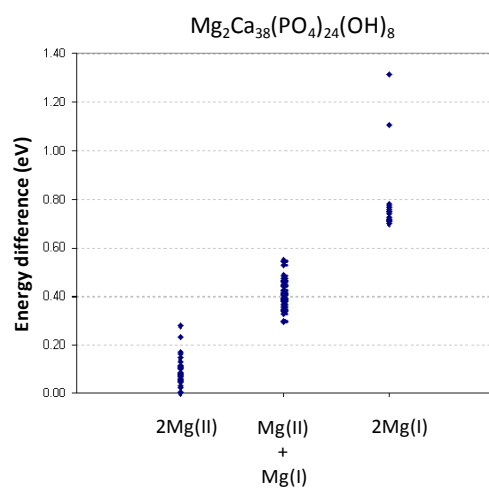
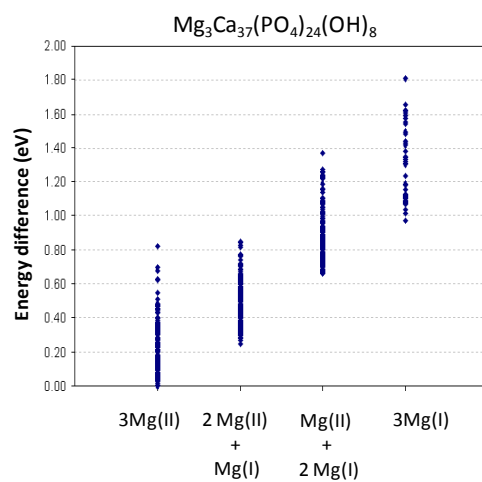


Figure 9

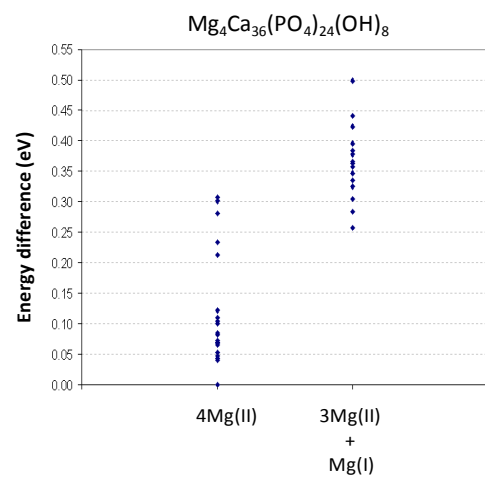
a/ 5 mol % Mg



b/ 7.5 mol % Mg



c/ 10 mol % Mg



## Tables

**Table 1** Unit cell parameters of stoichiometric HA and singly substituted Mg-HA in a (1 x 2 x 1) supercell, and energy differences between the different structures, calculated by DFT

|                                       | HA(exp)<br>[63] | HA(calc) | <b>Mg in<br/>Ca(IIa)</b> | Mg in<br>Ca(IIb) | Mg in<br>Ca(IIc) | Mg in<br>Ca(Ia) | Mg in<br>Ca(Ib) |
|---------------------------------------|-----------------|----------|--------------------------|------------------|------------------|-----------------|-----------------|
| <b>Energy<br/>difference<br/>(eV)</b> | ---             | ---      | <b>0</b>                 | 0.10             | 0.13             | 0.14            | 0.14            |
| Cell<br>volume( $\text{\AA}^3$ )      | 1224.30         | 1230.09  | <b>1218.25</b>           | 1218.99          | 1215.13          | 1214.98         | 1214.84         |
| a ( $\text{\AA}$ )                    | 9.43            | 9.40     | <b>9.34</b>              | 9.39             | 9.34             | 9.37            | 9.39            |
| 2b ( $\text{\AA}$ )                   | 18.86           | 18.81    | <b>18.76</b>             | 18.70            | 18.76            | 18.75           | 18.72           |
| c ( $\text{\AA}$ )                    | 6.88            | 6.95     | <b>6.95</b>              | 6.94             | 6.95             | 6.92            | 6.92            |
| $\alpha$ ( $^\circ$ )                 | 90              | 90       | <b>90</b>                | 90               | 90               | 90              | 90              |
| $\beta$ ( $^\circ$ )                  | 90              | 90       | <b>90</b>                | 90               | 90               | 90              | 90              |
| $\gamma$ ( $^\circ$ )                 | 120             | 120      | <b>120</b>               | 120              | 120              | 120             | 120             |

**Table 2.** Calculated NMR parameters for stoichiometric and Mg-substituted HA structures. Isotropic chemical shifts are given in ppm. All quadrupolar coupling constants  $C_Q$  are given in MHz, as absolute values. The P, H, Ca(I) and Ca(II) parameters are averaged over the *all* the different sites of the structure, and the corresponding standard deviations are given. The intrinsic error bars for these calculated NMR parameters can be found in the computational details.

| NMR parameters                       | DFT optimized structures<br>(1 x 2 x 1) supercell |                |                |                |                |                | Interatomic potential optimized structures<br>(1 x 2 x 2) supercell |                |                |
|--------------------------------------|---|----------------|----------------|----------------|----------------|----------------|---|----------------|----------------|
|                                      | HA  | Mg in Ca(IIa)  | Mg in Ca(IIb)  | Mg in Ca(IIc)  | Mg in Ca(Ia)   | Mg in Ca(Ib)   | HA  | Mg in Ca(I)    | Mg in Ca(II)   |
| $\delta_{\text{iso}}(\text{H})$      | 0.2 $\pm$ 0.01                                    | 0.4 $\pm$ 0.2  | 0.4 $\pm$ 0.2  | 0.5 $\pm$ 0.4  | 0.7 $\pm$ 0.8  | 0.8 $\pm$ 1.2  | 0.3 $\pm$ 0.05  | 0.4 $\pm$ 0.6  | 0.3 $\pm$ 0.2  |
| $\delta_{\text{iso}}(\text{P})$      | 3.3 $\pm$ 0.4                                     | 3.6 $\pm$ 1.7  | 3.5 $\pm$ 1.1  | 3.4 $\pm$ 1.3  | 3.5 $\pm$ 0.9  | 3.2 $\pm$ 1.0  | 2.8 $\pm$ 0.4   | 2.8 $\pm$ 1.0  | 2.6 $\pm$ 0.8  |
| $\delta_{\text{iso}}(\text{Ca(I)})$  | 9.4 $\pm$ 0.3                                     | 15.6 $\pm$ 3.9 | 12.2 $\pm$ 5.0 | 12.3 $\pm$ 6.8 | 11.3 $\pm$ 7.1 | 11.9 $\pm$ 8.7 | 12.1 $\pm$ 1.4  | 12.0 $\pm$ 4.9 | 13.1 $\pm$ 2.4 |
| $C_Q(\text{Ca(I)})$                  | 2.0 $\pm$ 0.2                                     | 2.2 $\pm$ 0.2  | 2.0 $\pm$ 0.4  | 2.0 $\pm$ 0.3  | 1.9 $\pm$ 0.6  | 1.9 $\pm$ 0.4  | 2.0 $\pm$ 0.2   | 2.0 $\pm$ 0.3  | 2.0 $\pm$ 0.2  |
| $\eta(\text{Ca(I)})$                 | 0.8 $\pm$ 0.1                                     | 0.5 $\pm$ 0.3  | 0.7 $\pm$ 0.3  | 0.8 $\pm$ 0.2  | 0.7 $\pm$ 0.3  | 0.7 $\pm$ 0.1  | 0.8 $\pm$ 0.1   | 0.8 $\pm$ 0.2  | 0.7 $\pm$ 0.2  |
| $\delta_{\text{iso}}(\text{Ca(II)})$ | 28.9 $\pm$ 1.5                                    | 26.6 $\pm$ 5.2 | 27.9 $\pm$ 5.5 | 27.8 $\pm$ 4.0 | 27.4 $\pm$ 3.6 | 27.7 $\pm$ 4.1 | 29.9 $\pm$ 1.9  | 30.0 $\pm$ 3.6 | 29.9 $\pm$ 3.8 |
| $C_Q(\text{Ca(II)})$                 | 1.7 $\pm$ 0.1                                     | 1.7 $\pm$ 0.3  | 1.7 $\pm$ 0.2  | 1.7 $\pm$ 0.2  | 2.0 $\pm$ 0.3  | 2.0 $\pm$ 0.3  | 1.8 $\pm$ 0.1   | 1.9 $\pm$ 0.3  | 1.8 $\pm$ 0.2  |
| $\eta(\text{Ca(II)})$                | 0.7 $\pm$ 0.1                                     | 0.6 $\pm$ 0.2  | 0.7 $\pm$ 0.2  | 0.8 $\pm$ 0.2  | 0.6 $\pm$ 0.3  | 0.6 $\pm$ 0.2  | 0.7 $\pm$ 0.1   | 0.7 $\pm$ 0.2  | 0.6 $\pm$ 0.2  |
| $\delta_{\text{iso}}(\text{Mg})$     |   | -18.2          | -20.5          | -24.6          | -23.4          | -23.8          |   | -11.2          | -7.6           |
| $C_Q(\text{Mg})$                     |   | 10.6           | 12.0           | 8.8            | 5.4            | 7.4            |   | 7.5            | 8.6            |
| $\eta(\text{Mg})$                    |   | 0.2            | 0.3            | 0.1            | 0.5            | 0.9            |   | 0.9            | 0.6            |



## References

1. Elliott JC. Studies in Inorganic Chemistry Volume 18: Structure and Chemistry of the Apatites and Other Calcium Orthophosphates, 1994.
2. Dorozhkin SV. Calcium orthophosphates. *Journal of Materials Science* 2007;42(4):1061-1095.
3. Roberts NB, Walsh HPJ, Klenerman L, Kelly SA, Helliwell TR. Determination of elements in human femoral bone using inductively coupled plasma atomic emission spectrometry and inductively coupled plasma mass spectrometry. *Journal of Analytical Atomic Spectrometry* 1996;11(2):133-138.
4. Heaney RP. Role of dietary sodium in osteoporosis. *Journal of the American College of Nutrition* 2006;25(3, Suppl.):271S-276S.
5. Featherstone JDB. Prevention and reversal of dental caries: role of low level fluoride. *Comm Dent Oral Epidemiol* 1999;27(2):31.
6. Robinson C, Weatherell JA, Hallsworth AS. Distribution of magnesium in mature human enamel. *Caries Research* 1981;15(1):70-77.
7. Robinson C, Weatherell JA. Magnesium in bone and tooth. *Metal Ions in Biological Systems* 1990;26(Compend. Magnesium Its Role Biol., Nutr., Physiol.):489-504.
8. Landi E, Tampieri A, Mattioli-Belmonte M, Celotti G, Sandri M, Gigante A, et al. Biomimetic Mg- and MgCO<sub>3</sub>-substituted hydroxyapatites: synthesis characterization and in vitro behaviour. *Journal of the European Ceramic Society* 2006;26(13):2593-2601.
9. Rude RK, Gruber HE. Magnesium deficiency and osteoporosis: animal and human observations. *Journal of Nutritional Biochemistry* 2004;15(12):710-716.
10. Luoma H. The role of magnesium in the aetiology and prevention of caries: some new findings and implications. *Magnesium research : official organ of the International Society for the Development of Research on Magnesium* 1988;1(3-4):223-230.
11. Gomes S, Renaudin G, Jallot E, Nedelec JM. Structural Characterization and Biological Fluid Interaction of Sol-Gel-Derived Mg-Substituted Biphasic Calcium Phosphate Ceramics. *ACS Applied Materials & Interfaces* 2009;1(2):505-513.
12. Landi E, Logroscino G, Proietti L, Tampieri A, Sandri M, Sprio S. Biomimetic Mg-substituted hydroxyapatite: from synthesis to in vivo behavior. *Journal of Materials Science: Materials in Medicine* 2008;19(1):239-247.
13. Bigi A, Falini G, Foresti E, Gazzano M, Ripamonti A, Roveri N. Magnesium influence on hydroxyapatite crystallization. *Journal of Inorganic Biochemistry* 1993;49(1):69-78.
14. Suchanek WL, Byrappa K, Shuk P, Riman RE, Janas VF, TenHuisen KS. Preparation of magnesium-substituted hydroxyapatite powders by the mechanochemical-hydrothermal method. *Biomaterials* 2004;25(19):4647-4657.
15. Tampieri A, Celotti G, Landi E, Sandri M. Magnesium doped hydroxyapatite: synthesis and characterization. *Key Eng Mater* 2004;264-268(Pt. 3, Euro Ceramics VIII):2051-2054.
16. Mroz W, Bombalska A, Burdyska S, Jedynski M, Prokopiuk A, Budner B, et al. Structural studies of magnesium doped hydroxyapatite coatings after osteoblast culture. *Journal of Molecular Structure*;977(1-3):145-152.
17. Gibson IR, Bonfield W. Preparation and characterization of magnesium/carbonate co-substituted hydroxyapatites. *Journal of Materials Science: Materials in Medicine* 2002;13(7):685-693.
18. Bertinetti L, Drouet C, Combes C, Rey C, Tampieri A, Coluccia S, et al. Surface Characteristics of Nanocrystalline Apatites: Effect of Mg Surface Enrichment on Morphology, Surface Hydration Species, and Cationic Environments. *Langmuir* 2009;25(10):5647-5654.
19. Bertinetti L, Tampieri A, Landi E, Martra G, Coluccia S. Punctual investigation of surface sites of HA and magnesium-HA. *Journal of the European Ceramic Society* 2006;26(6):987-991.
20. Bigi A, Falini G, Foresti E, Gazzano M, Ripamonti A, Roveri N. Rietveld structure refinements of calcium hydroxylapatite containing magnesium. *Acta Crystallogr, Sect B: Struct Sci* 1996;B52(1):87-92.

21. Sprio S, Pezzotti G, Celotti G, Landi E, Tampieri A. Raman and cathodoluminescence spectroscopies of magnesium-substituted hydroxyapatite powders. *Journal of Materials Research* 2005;20(4):1009-1016.
22. Yasukawa A, Ouchi S, Kandori K, Ishikawa T. Preparation and characterization of magnesium-calcium hydroxyapatites. *J Mater Chem* 1996;6(8):1401-1405.
23. Bigi A, Boanini E, Capuccini C, Gazzano M. Strontium-substituted hydroxyapatite nanocrystals. *Inorganica Chimica Acta* 2007;360(3):1009-1016.
24. Bigi A, Foresti E, Marchetti F, Ripamonti A, Roveri N. Barium calcium hydroxyapatite solid solutions. *Journal of the Chemical Society, Dalton Transactions: Inorganic Chemistry (1972-1999)* 1984(6):1091-1093.
25. Tang Y, Chappell HF, Dove MT, Reeder RJ, Lee YJ. Zinc incorporation into hydroxylapatite. *Biomaterials* 2009;30(15):2864-2872.
26. Pizzala H, Caldarelli S, Eon J-G, Rossi AM, Laurencin D, Smith ME. A Solid-State NMR Study of Lead and Vanadium Substitution into Hydroxyapatite. *J Am Chem Soc* 2009;131(14):5145-5152.
27. Matsunaga K, Inamori H, Murata H. Theoretical trend of ion exchange ability with divalent cations in hydroxyapatite. *Physical Review B: Condensed Matter and Materials Physics* 2008;78(9):094101/094101-094101/094108.
28. Matsunaga K. First-principles study of substitutional magnesium and zinc in hydroxyapatite and octacalcium phosphate. *Journal of Chemical Physics* 2008;128(24):245101/245101-245101/245110.
29. Tamm T, Peld M. Computational study of cation substitutions in apatites. *Journal of Solid State Chemistry* 2006;179(5):1581-1587.
30. de Leeuw NH, Bowe JR, Rabone JAL. A computational investigation of stoichiometric and calcium-deficient oxy- and hydroxy-apatites. *Faraday Discussions* 2007;134:195-214.
31. Bertoni E, Bigi A, Cojazzi G, Gandolfi M, Panzavolta S, Roveri N. Nanocrystals of magnesium and fluoride substituted hydroxyapatite. *Journal of Inorganic Biochemistry* 1998;72(1,2):29-35.
32. Siegel R, Nakashima TT, Wasylishen RE. Sensitivity enhancement of NMR spectra of half-integer quadrupolar nuclei in the solid state via population transfer. *Concepts in Magnetic Resonance, Part A* 2005;26A(2):47-61.
33. Kwak H-T, Prasad S, Clark T, Grandinetti PJ. Enhancing sensitivity of quadrupolar nuclei in solid-state NMR with multiple rotor assisted population transfers. *Solid State Nuclear Magnetic Resonance* 2003;24(2 & 3):71-77.
34. Laurencin D, Wong A, Dupree R, Smith ME. Natural abundance  $^{43}\text{Ca}$  solid-state NMR characterization of hydroxyapatite: identification of the two calcium sites. *Magnetic Resonance in Chemistry* 2008;46(4):347-350.
35. Van Veenendaal E, Meier BH, Kentgens APM. Frequency stepped adiabatic passage excitation of half-integer quadrupolar spin systems. *Molecular Physics* 1998;93(2):195-213.
36. Lutz O, Schwenk A, Uhl A. Fourier transform nuclear magnetic resonance studies of magnesium-25 and calcium-43. *Zeitschrift fuer Naturforschung, Teil A: Astrophysik, Physik und Physikalische Chemie* 1975;30A(9):1122-1127.
37. Gervais C, Laurencin D, Wong A, Pourpoint F, Labram J, Woodward B, et al. New perspectives on calcium environments in inorganic materials containing calcium-oxygen bonds: A combined computational-experimental  $^{43}\text{Ca}$  NMR approach. *Chemical Physics Letters* 2008;464(1-3):42-48.
38. MacKenzie KJD, Smith ME. *Multinuclear Solid-State Nuclear Magnetic Resonance of Inorganic Materials*; Pergamon Press, Oxford, 2002.
39. Cahill LS, Hanna JV, Wong A, Freitas JCC, Yates JR, Harris RK, et al. Natural Abundance  $^{25}\text{Mg}$  Solid-State NMR of Mg Oxyanion Systems: A Combined Experimental and Computational Study. *Chem--Eur J* 2009;15(38):9785-9798, S9785/9781-S9785/9783.
40. Ravel B, Newville M. ATHENA, ARTEMIS, HEPHAESTUS: data analysis for x-ray absorption spectroscopy using IFEFFIT. *Journal of Synchrotron Radiation* 2005;12(4):537-541.

41. Klementev KV. Extraction of the fine structure from x-ray absorption spectra. *Journal of Physics D: Applied Physics* 2001;34(2):209-217.
42. Klementev KV. VIPER for Windows. freeware: [www.desy.de/~klmn/viper.html](http://www.desy.de/~klmn/viper.html).
43. Binsted N, Campbell JW, Gurman SJ, Stephenson PC. EXAFS Analysis programs. Warrington, UK: Daresbury Laboratory.
44. Sugiyama S, Minami T, Moriga T, Hayashi H, Koto K, Tanaka M, et al. Surface and bulk properties, catalytic activities and selectivities in methane oxidation on near-stoichiometric calcium hydroxyapatites. *J Mater Chem* 1996;6(3):459-464.
45. Skipper LJ, Sowrey FE, Pickup DM, Fitzgerald V, Rashid R, Drake KO, et al. Structural studies of bioactivity in sol-gel-derived glasses by X-ray spectroscopy. *Journal of Biomedical Materials Research, Part A* 2004;70A(2):354-360.
46. Laurencin D, Wong A, Chrzanowski W, Knowles JC, Qiu D, Pickup DM, et al. Probing the calcium and sodium local environment in bones and teeth using multinuclear solid state NMR and X-ray absorption spectroscopy. *Physical Chemistry Chemical Physics* 2010;12(5):1081-1091.
47. Rabone JAL, De Leeuw NH. Interatomic potential models for natural apatite crystals: Incorporating strontium and the lanthanides. *Journal of Computational Chemistry* 2006;27(2):253-266.
48. de Leeuw NH. Resisting the Onset of Hydroxyapatite Dissolution through the Incorporation of Fluoride. *J Phys Chem B* 2004;108(6):1809-1811.
49. Mostafa NY, Brown PW. Computer simulation of stoichiometric hydroxyapatite. Structure and substitutions. *Journal of Physics and Chemistry of Solids* 2007;68(3):431-437.
50. Ellis DE, Terra J, Warschkow O, Jiang M, Gonzalez GB, Okasinski JS, et al. A theoretical and experimental study of lead substitution in calcium hydroxyapatite. *Physical Chemistry Chemical Physics* 2006;8(8):967-976.
51. Ordejon P, Artacho E, Soler JM. Self-consistent order-N density-functional calculations for very large systems. *Phys Rev B* 1996 Apr 15;53(16):10441-10444.
52. Kohn W, Sham LJ. Self-Consistent Equations Including Exchange and Correlation Effects. *Phys Rev* 1965;140(4A):1133-&.
53. Perdew JP, Burke K, Ernzerhof M. Generalized gradient approximation made simple. *Phys Rev Lett* 1996 Oct 28;77(18):3865-3868.
54. Troullier N, Martins JL. Efficient Pseudopotentials for Plane-Wave Calculations .2. Operators for Fast Iterative Diagonalization. *Phys Rev B* 1991 Apr 15;43(11):8861-8869.
55. Anglada E, Soler JM, Junquera J, Artacho E. Systematic generation of finite-range atomic basis sets for linear-scaling calculations. *Phys Rev B* 2002 Nov 15;66(20):-.
56. Junquera J, Paz O, Sanchez-Portal D, Artacho E. Numerical atomic orbitals for linear-scaling calculations. *Phys Rev B* 2001 Dec 15;64(23):-.
57. Gale JD. GULP: A computer program for the symmetry-adapted simulation of solids. *Journal of the Chemical Society-Faraday Transactions* 1997;93(4):629-637.
58. Gale JD, Rohl AL. The General Utility Lattice Program (GULP). *Molecular Simulation* 2003;29(5):291-341.
59. Gale JD. GULP: Capabilities and prospects. *Zeitschrift Fur Kristallographie* 2005;220(5-6):552-554.
60. Born M, Huang K. Dynamical theory of crystal lattices. Oxford: Clarendon Press, 1954.
61. de Leeuw NH. A computer modelling study of the uptake and segregation of fluoride ions at the hydrated hydroxyapatite (0001) surface: introducing Ca-10(PO<sub>4</sub>)(6)(OH)(2) potential model. *Phys Chem Chem Phys* 2004 Apr 21;6(8):1860-1866.
62. Dick BG, Overhauser AW. Theory of the Dielectric Constants of Alkali Halide Crystals. *Physical Review* 1958;112(1):90-103.
63. Posner AS, Perloff A, Diorio AF. Refinement of the Hydroxyapatite Structure. *Acta Crystallographica* 1958;11(4):308-309.

64. Markovic M, Fowler BO, Tung MS. Preparation and comprehensive characterization of a calcium hydroxyapatite reference material. *Journal of Research of the National Institute of Standards and Technology* 2004;109(6):553-568.
65. Sudarsanan K, Young RA. Significant precision in crystal structural details: Holly Springs hydroxyapatite. *Acta Crystallographica, Section B: Structural Crystallography and Crystal Chemistry* 1969;25(Pt. 8):1534-1543.
66. de Leeuw NH. Local ordering of hydroxy groups in hydroxyapatite. *Chem Commun (Cambridge, U K)* 2001(17):1646-1647.
67. de Leeuw NH. Density functional theory calculations of local ordering of hydroxy groups and fluoride ions in hydroxyapatite. *Physical Chemistry Chemical Physics* 2002;4(15):3865-3871.
68. Stork L, Muller P, Dronskowski R, Ortlepp JR. Chemical analyses and X-ray diffraction investigations of human hydroxyapatite minerals from aortic valve stenoses. *Zeitschrift Fur Kristallographie* 2005;220(2-3):201-205.
69. Suetsugu Y, Tanaka J. Crystal growth and structure analysis of twin-free monoclinic hydroxyapatite. *Journal of Materials Science: Materials in Medicine* 2002;13(8):767-772.
70. Pickard CJ, Mauri F. All-electron magnetic response with pseudopotentials: NMR chemical shifts. *Physical Review B: Condensed Matter and Materials Physics* 2001;63(24):245101/245101-245101/245113.
71. PARATEC (PARALLEL Total Energy Code) by Pfrommer B., Raczkowski D., Canning A., Louie S.G.; Lawrence Berkeley National Laboratory (with contributions from Mauri F., Cote M., Yoon Y., Pickard C. and Heynes P.). For more information see [www.nersc.gov/projects/paratec](http://www.nersc.gov/projects/paratec) <<http://www.nersc.gov/projects/paratec>>.
72. Troullier N, Martins JL. Efficient pseudopotentials for plane-wave calculations. *Phys Rev B: Condens Matter* 1991;43(3):1993-2006.
73. Kleinman L, Bylander DM. Efficacious form for model pseudopotentials. *Physical Review Letters* 1982;48(20):1425-1428.
74. Gervais C, Profeta M, Lafond V, Bonhomme C, Azais T, Mutin H, et al. Combined ab initio computational and experimental multinuclear solid-state magnetic resonance study of phenylphosphonic acid. *Magnetic Resonance in Chemistry* 2004;42(5):445-452.
75. Schimmel HG, Huot J, Chapon LC, Tichelaar FD, Mulder FM. Hydrogen Cycling of Niobium and Vanadium Catalyzed Nanostructured Magnesium. *J Am Chem Soc* 2005;127(41):14348-14354.
76. Pallister PJ, Moudrakovski IL, Ripmeester JA. Mg-25 ultra-high field solid state NMR spectroscopy and first principles calculations of magnesium compounds. *Physical Chemistry Chemical Physics* 2009;11(48):11487-11500.
77. Salager E, Day GM, Stein RS, Pickard CJ, Elena B, Emsley L. Powder Crystallography by Combined Crystal Structure Prediction and High-Resolution <sup>1</sup>H Solid-State NMR Spectroscopy. *J Am Chem Soc*;132(8):2564-2566.
78. Bonhomme C, Gervais C, Coelho C, Pourpoint F, Azais T, Bonhomme-Courty L, et al. New perspectives in the PAW/GIPAW approach: J P-O-Si coupling constants, antisymmetric parts of shift tensors and NQR predictions. *Magnetic Resonance in Chemistry* 2010;doi:10.1002/mrc.2635.
79. Yesinowski JP, Eckert H. Hydrogen environments in calcium phosphates: proton MAS NMR at high spinning speeds. *J Am Chem Soc* 1987;109(21):6274-6282.
80. Isobe T, Nakamura S, Nemoto R, Senna M, Sfihi H. Solid-state double nuclear magnetic resonance study of the local structure of calcium phosphate nanoparticles synthesized by a wet-mechanochemical reaction. *J Phys Chem B* 2002;106(20):5169-5176.
81. Badraoui B, Bigi A, Debbabi M, Gazzano M, Roveri N, Thouvenot R. X-ray powder diffraction and solid-state NMR investigations in cadmium-lead hydroxyapatites. *Eur J Inorg Chem* 2001(5):1261-1267.

82. Badraoui B, Bigi A, Debbabi M, Gazzano M, Roveri N, Thouvenot R. Physicochemical properties and structural refinement of strontium-lead hydroxyapatites. *Eur J Inorg Chem* 2002(7):1864-1870.
83. Bryce DL. Calcium binding environments probed by  $^{43}\text{Ca}$  NMR spectroscopy. *Dalton Trans* 2010;39(37):8577-8836.
84. Bryce DL, Bultz EB, Aebi D. Calcium-43 Chemical Shift Tensors as Probes of Calcium Binding Environments. Insight into the Structure of the Vaterite  $\text{CaCO}_3$  Polymorph by  $^{43}\text{Ca}$  Solid-State NMR Spectroscopy. *J Am Chem Soc* 2008;130(29):9282-9292.
85. Dupree R, Howes AP, Kohn SC. Natural abundance solid state  $^{43}\text{Ca}$  NMR. *Chemical Physics Letters* 1997;276(5,6):399-404.
86. Cormier L, Neuville DR. Ca and Na environments in  $\text{Na}_2\text{O}-\text{CaO}-\text{Al}_2\text{O}_3-\text{SiO}_2$  glasses: influence of cation mixing and cation-network interactions. *Chemical Geology* 2004;213(1-3):103-113.
87. Harries JE, Hukins DWL, Hasnain SS. Analysis of the EXAFS spectrum of hydroxyapatite. *J Phys C: Solid State Phys* 1986;19(34):6859-6872.
88. Lipton AS, Heck RW, Primak S, McNeill DR, Wilson DM, Ellis PD. Characterization of  $\text{Mg}^{2+}$  Binding to the DNA Repair Protein Apurinic/Apyrimidic Endonuclease 1 via Solid-State  $^{25}\text{Mg}$  NMR Spectroscopy. *J Am Chem Soc* 2008;130(29):9332-9341.
89. Perez-Huerta A, Cusack M, Janousch M, Finch AA. Influence of crystallographic orientation of biogenic calcite on in situ Mg XANES analyses. *Journal of Synchrotron Radiation* 2008;15(6):572-575.
90. Politi Y, Batchelor DR, Zaslansky P, Chmelka BF, Weaver JC, Sagi I, et al. Role of Magnesium Ion in the Stabilization of Biogenic Amorphous Calcium Carbonate: A Structure-Function Investigation. *Chem Mater* 2010;22(1):161-166.
91. Jupe AC, Cockcroft JK, Barnes P, Colston SL, Sankar G, Hall C. The site occupancy of Mg in the brownmillerite structure and its effect on hydration properties: an x-ray/neutron diffraction and EXAFS study. *Journal of Applied Crystallography* 2001;34(1):55-61.
92. Mayer I, Schlam R, Featherstone FDB. Magnesium-containing carbonate apatites. *Journal of Inorganic Biochemistry* 1997;66(1):1-6.
93. Grau-Crespo R, Hamad S, Catlow CRA, de Leeuw NH. Symmetry-adapted configurational modelling of fractional site occupancy in solids. *Journal of Physics-Condensed Matter* 2007 Jun 27;19(25):265201.